ENTRY GUIDANCE FOR THE REUSABLE LAUNCH VEHICLE

FINAL REPORT

(January 5, 1997 – July 6, 1999)

Research Supported by

NASA Marshall Space Flight Center

Grant NAG8-1289

NASA Technical Officer: John M. Hanson

Principal Investigator: Ping Lu

Department of Aerospace Engineering and Engineering Mechanics

Iowa State University

Ames, IA 50011-3231

ABSTRACT

The X-33 Advanced Technology Demonstrator is a half-scale prototype developed to test the key technologies needed for a full-scale single-stage reusable launch vehicle (RLV). The X-33 is a suborbital vehicle that will be launched vertically, and land horizontally. The goals of this research were to develop an alternate entry guidance scheme for the X-33 in parallel to the actual X-33 entry guidance algorithms, provide comparative and complementary study, and identify potential new ways to improve entry guidance performance. Toward these goals, the nominal entry trajectory is defined by a piecewise linear drag-acceleration-versus-energy profile, which is in turn obtained by the solution of a semi-analytical parameter optimization problem. The closed-loop guidance is accomplished by tracking the nominal drag profile with primarily bank-angle modulation on-board. The bank-angle is commanded by a single full-envelope nonlinear trajectory control law. Near the end of the entry flight, the guidance logic is switched to heading control in order to meet strict conditions at the terminal area energy management interface. Two methods, one on ground-track control and the other on heading control, were proposed and examined for this phase of entry guidance where lateral control is emphasized. Trajectory dispersion studies were performed to evaluate the effectiveness of the entry guidance algorithms against a number of uncertainties including those in propulsion system, atmospheric properties, winds, aerodynamics, and propellant loading. Finally, a new trajectory-regulation method is introduced at the end as a promising precision entry guidance method. The guidance principle is very different and preliminary application in X-33 entry guidance simulation showed high precision that is difficult to achieve by existing methods.

TABLE OF CONTENTS

1. Introduction

The X-33 vehicle, a half-scale prototype for reusable launch vehicle (RLV), is an unmanned suborbital autonomous vehicle (Fig. 1). The primary technical goals of the X-33 program are to develop and test key technologies needed for the next-generation of single-stage-to-orbit RLV, including structure, thermal protection system, linear aerospike engine, aerodynamic prediction, and control and guidance. During the flight tests projected to begin in 2000, the X-33 will be launched vertically from Edwards Air Force Base (AFB), California, and land horizontally at sites in Utah or Montana. The flight trajectories will cover a range of Mach numbers for various test objectives such as maximum entry catalytic heating, maximum entry integrated heat load and maximum delay of transition to turbulent flow.

The flight sequence of the X-33 will be powered ascent till the main engine cutoff (MECO) at at an altitude of about 190,000 ft, followed by a short transition phase, then entry flight to the terminal area energy management (TAEM) interface at Mach 3 and 30 nm from the heading alignment cylinder near the end of the runway, finally the approach and landing phase from the TAEM interface to the runway. Thus a major portion of the flight is under the control of the entry guidance system. The entry guidance is concerned with guiding the X-33 in entry flight while satisfying a number of inflight constraints and delivering the vehicle to the TAEM interface with required conditions. The effectiveness of the entry guidance scheme is a key factor in assuring the success of the flight tests. Because of the unique trajectory pattern of the X-33 (i.e., entry flight immediately follows ascent), the entry flight is directly coupled with ascent, and any trajectory dispersions in the ascent phase will be propagated to and amplified by the entry flight. Therefore not only should the X-33 entry guidance be accurate in a nominal situation, but also must be sufficiently adaptive and robust in off-nominal cases.

The entry guidance design for the X-33 follows the principle of the Space Shuttle entry guidance.[1] But significant differences exist in methodology, algorithms and implementation.[2, 3] In this framework, the tasks in entry guidance design include the design of a nominal entry trajectory, a reference drag profile used for on-board guidance, trajectory tracking control law, and algorithms to ensure the satisfaction of the TAEM conditions. The rest of this report addresses each of these aspects.

2. Entry Trajectory Design

The nominal entry trajectory provides a reference and benchmark for the entry flight. The design of such a trajectory is done off-line, and a number of trajectory constraints must be enforced in the process. Different performance indices, depending on the mission objectives, may also optimized. For the X-33, ascent and entry trajectories are designed simultaneously because of the direct coupling between the two phases. Although nominal trajectory design is not the emphasis of this research, it is needed to validate our subsequent development. For this purpose, an trajectory design approach is described in the following.

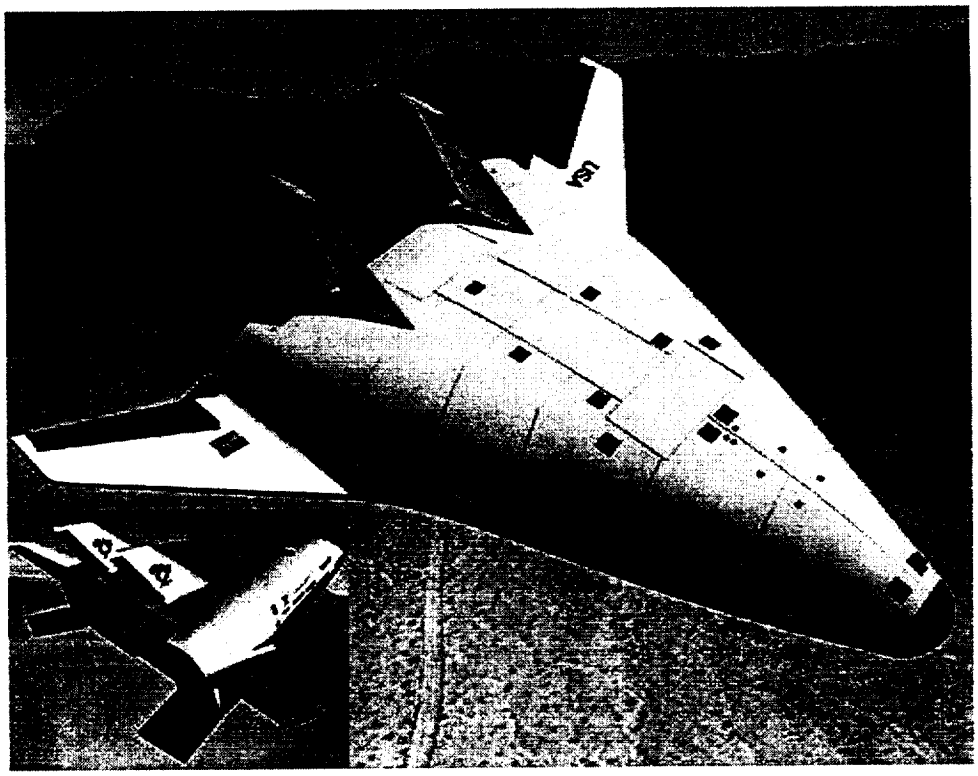

Figure 1: The X-33 Advanced Technology Demonstrator

2.1 Formulation

We begin with the point-mass dimensionless equations of 3-D motion over a spherical, rotating Earth[4]

$$\dot{r} = V \sin\gamma \tag{1}$$

$$\dot{\theta} = \frac{V \cos\gamma \sin\psi}{r \cos\phi} \tag{2}$$

$$\dot{\phi} = \frac{V \cos\gamma \cos\psi}{r} \tag{3}$$

$$\dot{V} = -D - \frac{\sin\gamma}{r^2} + \Omega^2 r \cos\phi(\sin\gamma\cos\phi - \cos\gamma\sin\phi\cos\psi) \tag{4}$$

$$\begin{aligned}\dot{\gamma} &= \frac{1}{V}[L\cos\sigma + \left(V^2 - \frac{1}{r}\right)\frac{\cos\gamma}{r} + 2\Omega V\cos\phi\sin\psi \\ &+ \Omega^2 r\cos\phi(\cos\gamma\cos\phi + \sin\gamma\cos\psi\sin\phi)]\end{aligned} \tag{5}$$

$$\begin{aligned}\dot{\psi} &= \frac{1}{V}[\frac{L\sin\sigma}{\cos\gamma} + \frac{V^2}{r}\cos\gamma\sin\psi\tan\phi - 2\Omega V(\tan\gamma\cos\psi\cos\phi - \sin\phi) \\ &+ \frac{\Omega^2 r}{\cos\gamma}\sin\psi\sin\phi\cos\phi]\end{aligned} \tag{6}$$

where r is the radial distance from the center of the earth to the X-33, normalized by the radius of the earth $R_0 = 6378$ km (20,925,673 ft). The longitude and latitude are θ and ϕ,

respectively. The earth-relative velocity V is normalized by $\sqrt{g_0 R_0}$ with $g_0 = 9.81$ m/sec^2 (32.185 ft/sec^2). D and L are aerodynamic accelerations in g's. Ω is the rotation rate of the earth normalized by $\sqrt{g_0/R_0}$. γ is the flight path angle and σ the bank angle. The velocity azimuth angle ψ is measured from the North in a clockwise direction. The differentiation is with respect to the dimensionless time $\tau = t/\sqrt{R_0/g_0}$.

The conditions at the end of the transition phase are determined by the ascent trajectory and transition guidance, and are considered the given initial conditions for the entry trajectory. The terminal conditions for entry flight are specified at the TAEM interface. For trajectory optimization purposes, the location of a target TAEM point and other conditions at this point are given

$$\begin{aligned} r(\tau_f) = r_f,\ \theta(\tau_f) = \theta_f,\ \phi(\tau_f) = \phi_f, \\ V(\tau_f) = V_f,\ \gamma_{min} \le \gamma(\tau_f) \le \gamma_{max},\ \psi(\tau_f) = \psi_f \end{aligned} \tag{7}$$

where r_f is at an altitude of about 25 km and V_f corresponds to about Mach 3. θ_f and ϕ_f are determined by the landing site, and the typical γ_f is between -11 *deg* to -15 *deg*. The velocity azimuth ψ_f is determined by the requirement that the vehicle should be heading directly to the HAC at the TAEM interface. This is required because the X-33 would not have enough time to correct the heading before it reaches the HAC if the heading is not properly oriented at the TAEM interface. In addition, the following trajectory constraints are imposed

$$|L\cos\alpha + D\sin\alpha| \le n_{z_{max}} \tag{8}$$

$$\bar{q} \le \bar{q}_{max} \tag{9}$$

$$\dot{Q}_s \le \dot{Q}_{max} \tag{10}$$

$$\left(\frac{1}{r} - V^2\right)\frac{1}{r} - L \le 0 \tag{11}$$

where Eq. (8) is a constraint on the acceleration in the body-normal direction; Eq. (9) is on dynamic pressure $\bar{q}$; and Eq. (10) is on heat rate $\dot{Q}_s$ at a stagnation point. Multiple heat rate constraints for several stagnation points can be imposed, although only one is used in this work. In this study, $n_{z_{max}} = 2.5$ (g), $\bar{q}_{max} = 11{,}970$ N/m^2 (250 psf), and $\dot{Q}_{max} = 431{,}259$ W/m^2 (38 BTU/sec-ft^2) are used. The last constraint (11) is called the equilibrium glide constraint, obtained by setting $\gamma = \dot{\gamma} = 0$ in Eq. (5) with $\sigma = 0$ and neglecting Ω, although other nonzero constant σ and γ may also be used to achieve equilibrium glide. Such a constraint is useful in reducing the altitude oscillation along the entry trajectory for an orbital vehicle[1]. For the X-33, this constraint is not as critical, particularly for short-range entry flight. Nonetheless, it is still retained here because it provides a convenient lower bound on the drag acceleration which will be used later.

In the following design of the nominal entry trajectory, the angle of attack α is scheduled as a function of velocity, beginning at large value (40–45 degrees at 4000 m/sec and above) and gradually reducing to 8–15 degrees at the TAEM point. The bank angle σ is modulated to control the trajectory. Therefore in this section σ is parametrized as a piecewise linear function of time. The nodal values of the parametrization of σ and the flight time τ_f are

found to satisfy the TAEM condition (7), the inflight constraints (8-10), and minimize a performance index

$$J = \int_0^{\tau_f} \sqrt{\rho} V^3 d\tau \tag{12}$$

where $\rho = 1.752 e^{-R_0(r-1)/6700}$ (kg/m^3) is a reasonably good approximation to the 1976 U.S. standard atmosphere in the altitude range of interest to entry flight[5]. The performance index (12) is proportional to the accumulated heat load per unit area at the stagnation point. It should be noted here that other performance indices such as

$$J = \int_0^{\tau_f} \rho V^3 d\tau \tag{13}$$

may also be used. In this case the above integrand is proportional to the average heat rate on the surface of the vehicle, and the performance index is thus proportional to the total heat load of the vehicle. We have found that the choice of different performance indices has relatively minor effect on the final trajectory. This result is due to the fact that the trajectory is already tightly constrained by the TAEM conditions and the constraints Eqs. (8-11), therefore little room is available for significant optimization of any performance index. A performance index mostly serves the purpose of facilitating the search for a feasible trajectory using an optimization algorithm. For comparison of the results obtained later from piecewise linear drag profiles which uses Eq. (12) as the performance index, we shall use Eq. (12) in the numerical solutions.

2.2 Numerical Solutions

To solve the above parameter optimization problem using a nonlinear programming algorithm, each of the constraints (8-11), represented by $p_i(\tau) \leq 0,\ \forall \tau \in [0, \tau_f],\ i = 1, ..., 4$, is converted into a terminal inequality constraint by

$$w_i(\tau_f) \leq 0, \quad \text{where } \dot{w}_i = \max\{\delta, p_i\}, \text{ and } w_i(0) = 0 \tag{14}$$

where $\delta < 0$ is a very small constant (e.g., -10^{-6}). The reason for having δ instead of 0 is that the optimization algorithm we used treats any inequality constraint $w_i \leq 0$ as an active constraint even when $w_i = 0$, and attempts to compute the gradient of w_i. If $\delta = 0$ in Eq. (14), $w_i \leq 0$ will always be considered active even if $p_i(\tau) < 0$ for all $\tau \in [0, \tau_f]$. When the algorithm computes the gradient of w_i in this case, it will find that the gradient is zero, which causes premature termination of the optimization process.

The optimization algorithm used is a state-of-the-art sequential quadratic programming code developed by Zhou, Tits, and Lawrence, called FFSQP (FORTRAN Feasible Sequential Quadratic Programming)[6]. FFSQP proceeds by first finding a feasible solution that satisfies all the inequality constraints, if the user-provided initial point is infeasible. Then it generates the successive iterates which all satisfy the inequality constraints. This feature is particularly useful for highly constrained problems such as the current one, where providing a feasible starting point by trial and error is nearly impossible.

For a set of nodal values in the σ-parametrization and the final time τ_f which are now optimization parameters, the trajectory is obtained by numerically integrating Eqs. (1)-(6). The aerodynamic coefficients C_L and C_D for the X-33, given in tabulated data as functions

of Mach number and angle of attack, are found by table lookup. The speed of sound is also found by table lookup of the data from the 1976 U.S. Standard Atmosphere. The TAEM conditions (7) and inflight constraints (14) constitute the nonlinear equality and inequality constraints of the parameter optimization problem. FFSQP was used to find the optimal parameters which in turn determine the optimal trajectory. A total of 20 parameters were used, and finite differences were employed for gradient computation. The constraints were satisfied to the accuracy of 10^{-6}.

Since the X-33 vehicle and trajectory data were continuously updated while this research was being conducted, the numerical results in this report used some early vehicle data and trajectory information for the X-33. But the results still represent qualitatively what would be expected for the X-33.

Figure 2 shows the ground tracks of two entry trajectories of the X-33, one with a MECO velocity of Mach 14.2 for landing at Malmstrom AFB in Montana, and the other with a MECO velocity of Mach 9.35 for landing at Michael Army Air Field (AAF) in Utah. The trajectory to Malmstrom AFB has a tight turn at the end to meet a specified azimuth angle condition at TAEM. Figure 3 illustrates the bank angle histories along the two trajectories. The trajectories in the velocity-altitude space are depicted in Fig. 3 together with the four trajectory constraints boundaries (8-11). Note that the equilibrium glide constraint (11) was not imposed for the trajectory to Michael AAF because it was a relatively short trajectory. A characteristic of the trajectories is that every imposed constraint became active at one point or another, which underscores the importance of these constraints in this problem.

The computation required for these trajectories is very intensive, largely because of the highly constrained nature of the trajectories. Since portions of the trajectories lie on the constraint boundaries as seen in Fig. 3, the search steps had to be kept small in order not to violate these constraints. With twenty parameters and finite differences for gradient computation, the number of trajectory integrations needed to obtain convergence is on the order of 40,000, which translates into over ten CPU hours on a DEC 3000/300L Alpha workstation.

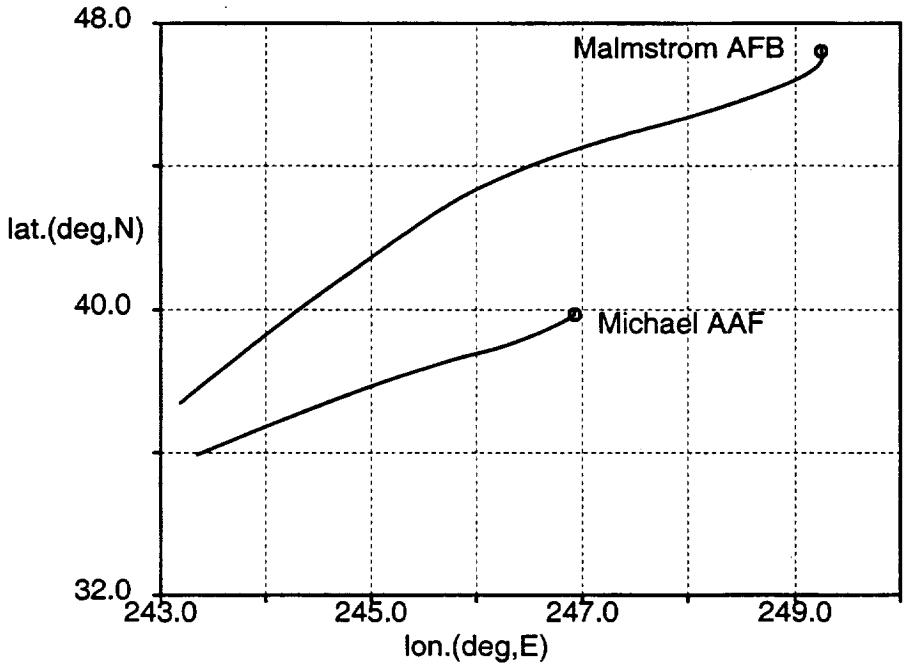

Figure 2: Ground tracks of the X-33 entry trajectories

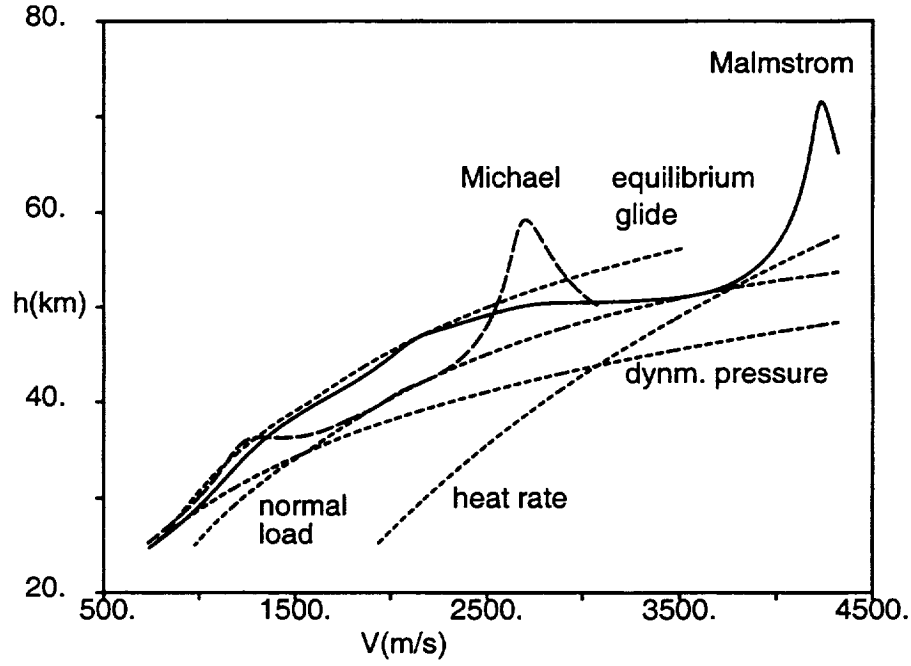

Figure 3: Entry trajectories to Michael AAF and Malmstrom AFB

3. Reference Drag Profiles

While the nominal 3-D trajectory obtained in above provides a good understanding of the entry flight, it is not directly used on-board in the Shuttle and X-33 entry guidance (a quite different precision entry guidance method that will be briefly introduced as future work in Section 7 will directly use the 3-D reference trajectory though). Instead, the essential features of the reference trajectory are embed in the drag acceleration profile extracted from the trajectory, and this drag profile is used a the reference and tracked on-board.[1, 2, 3]

Derivation of the reference drag profile from the 3-D nominal trajectory necessitates intensive computation as pointed out at the end of the preceding section. This research takes a different approach [7, 8] in which the reference drag profile is obtained by solving a semi-analytical parameter optimization problem. With appropriate formulation, the obtained drag profiles are very close to the ones extracted from the 3-D trajectories resulted from intensive trajectory optimization, but the process is much more efficient and takes negligible computation time. This high efficiency not only is much welcomed for off-line analysis and design, but also is potentially useful for redesign of the drag profile on-board .

3.1 Determination of Drag Profiles via Parameter Optimization

In scheduling the drag profile, the negative of the dimensionless specific energy

$$e = \frac{1}{r} - \frac{V^2}{2} \tag{15}$$

Note that by this definition e is monotonically increasing to almost unity along the entry trajectory. Let e_0 and e_f be the prescribed energy levels at the beginning of the entry flight and at the TAEM interface, respectively. Divide the interval $[e_0, e_f]$ into $n-1$ subintervals by the points $\{e_1, e_2, ..., e_n\}$ with $e_1 = e_0$ and $e_n = e_f$. In each interval $[e_i, e_{i+1}]$, $i = 1, ..., n-1$, let the desired drag acceleration be parametrized by a linear function of e

$$D(e) = a_i(e - e_i) + b_i \tag{16}$$

where

$$a_i = \frac{D_{i+1} - D_i}{e_{i+1} - e_i}, \quad b_i = D_i \tag{17}$$

The values of D_i, $i = 2, \ldots, n-1$, are to be determined (D_1 and D_n are determined by the initial and final conditions). For a given entry α-profile, all the constraints (8-11) at each node e_i can be converted in terms of D and e and expressed in the D-e space as the constraints on D_i

$$D_{min}(e_i) \leq D_i \leq D_{max}(e_i), \quad i = 2, ..., n-1 \tag{18}$$

If the variation of C_D is ignored, the performance index Eq. (12) can be shown to be proportional to

$$J^* = \int_{e_0}^{e_f} \sqrt{\frac{1-e}{D(e)}}\, de = \sum_{i=1}^{n-1} \Delta J_i \tag{19}$$

where

$$\Delta J_i = \begin{cases} (1/a_i)\left(\sqrt{D_{i+1}(1-e_{i+1})} - \sqrt{D_i(1-e_i)}\right) - \left[(a_i+d_i)/\sqrt{a_i^3}\right] \\ \times \left(\tan^{-1}\sqrt{a_i(1-e_{i+1})/D_{i+1}} - \tan^{-1}\sqrt{a_i(1-e_i)/D_i}\right), \quad a_i > 0; \\ (2/3\sqrt{D_i})\left(\sqrt{(1-e_i)^3} - \sqrt{(1-e_{i+1})^3}\right), \qquad a_i = 0; \\ (1/a_i)\left(\sqrt{D_{i+1}(1-e_{i+1})} - \sqrt{D_i(1-e_i)}\right) + \left[(a_i+d_i)/\sqrt{-a_i^3}\right] \\ \times \left(\ln|\sqrt{-a_i(1-e_{i+1})} - \sqrt{D_{i+1}}\,| - \ln|\sqrt{-a_i(1-e_i)} - \sqrt{D_i}\,|\right), \; a_i < 0. \end{cases} \tag{20}$$

The requirement of reaching the TAEM point ($\theta(\tau_f) = \theta_f$ and $\phi(\tau_f) = \phi_f$) is replaced by the requirement that the downrange distance traveled by flying the drag profile be equal to that from the beginning of the entry flight to the TAEM point. The downrange distance along a trajectory with drag profile $D(e)$ is given by[7]

$$s = \int_{e_0}^{e_f} \frac{\cos\gamma}{D(e)} de \tag{21}$$

When the drag profile is defined by the piecewise linear parametrization Eq. (16), the downrange distance can be analytically obtained, with the approximation of $\cos\gamma \approx 1$, as

$$s = \sum_{i=1}^{n-1} \Delta s_i \tag{22}$$

where

$$\Delta s_i = \begin{cases} (1/a_i)\ln(D_{i+1}/D_i), & a_i \neq 0 \\ (1/D_i)(e_{i+1}-e_i), & a_i = 0 \end{cases} \tag{23}$$

The design of an optimal entry trajectory now becomes a parameter optimization problem in which the values of the D_i's are to be found to minimize J^* in Eq. (19) while satisfying the inequality constraints (18) and

$$\sum_{i=1}^{n-1} \Delta s_i = s_f \tag{24}$$

In this formulation, however, it has been analytically predicted and numerically verified in Ref. [8] that the optimal drag profile has an undesirable feature of consisting of very rapid changes resulting from inherent discontinuities in the solution of the corresponding variational problem (see Ref. [8] for detail). Intuitively this phenomenon occurs because no vehicle dynamics are directly involved in this optimization process. To add more "damping" in the $D(e)$ profile, Ref. [8] suggests to include a regularization term in the cost function to reduce the rate of change of $D(e)$. The cost function for the parameter optimization problem thus becomes

$$\bar{J} = \sum_{i=1}^{n-1} \Delta J_i + \varepsilon \int_{e_0}^{e_f} \left[\frac{dD(e)}{de}\right]^2 de = \sum_{i=1}^{n-1} \Delta J_i + \varepsilon \sum_{i=1}^{n-1} \left[\frac{(D_{i+1}-D_i)^2}{e_{i+1}-e_i}\right] \tag{25}$$

where $\varepsilon > 0$ is a small constant ($\varepsilon = 5 \times 10^{-6}$ in this study). For the X-33, the initial entry trajectory following the transition phase is still ascending because of the positive flight path

angle. To count for this short ascent portion, the first few nodes in the drag profile (D_1–D_3) need to be specified accordingly. The last node D_n is also fixed, given the required altitude, Mach number and α at the TAEM interface. The rest of the parameters D_i are found by solving this parameter optimization problem.

Since no numerical integrations are required and the trajectory constraints are handled by the box constraints Eq. (18), the optimization problem can be solved much more efficiently as compared to the trajectory optimization approach in the preceding section. For the same number of parameters (twenty), the computation time required to solve the problem is over three orders of magnitude less compared to the trajectory optimization approach.

Figure 4 shows the comparison of the drag profile obtained here (in solid line) with the drag acceleration variation in dashed line along the numerical optimal trajectory shown in Fig. 3 for landing at Malmstrom AFB. The piecewise linear drag profile clearly captures the essential features of the numerical optimal solution at a small computation cost. The important difference at this point is that the numerical optimal trajectories can be designed at the expense of intensive computation to exactly meet the conditions for $\gamma(\tau_f)$ and $\psi(\tau_f)$ at TAEM. In contrast, the heading control along the trajectory defined by the drag profile has to be obtained by bank-angle reversals[1], and no direct control over $\gamma(\tau_f)$ is implemented, although an appropriately scheduled nominal α-program can result in a $\gamma(\tau_f)$ in the allowable range. Accurate satisfaction of the TAEM condition on $\psi(\tau_f)$, when required, will have to be to be achieved by other techniques which will be discussed later.

The chief benefits of the current approach are that the nominal entry trajectory can be designed very effectively, reliably and quickly, and the design process can be easily automated, thus saving significant amount of time and man power. This feature is probably particularly useful for an evolving test vehicle like the X-33.

3.2 Drag Profile Update

The reference drag profile D^* is designed based on the downrange distance requirement (24) at the beginning of the entry trajectory. Because of off-nominal dispersions and cross-range motion of the vehicle, the reference drag profile will need to be updated periodically on-board to null the downrange errors. The Shuttle uses a first-order approximation approach to adjust one segment of the drag profile at a time.[1] The piecewise linearity of the parametrization of D^* for the X-33 makes it a simple matter to update the entire D^* by scaling it with appropriate coefficients.

Define the range-to-go by

$$s_{to-go} = s_{hac} - s_{taem} \tag{26}$$

where s_{hac} is the downrange distance along the great circle from the current point to the HAC, and s_{taem} is a constant bias term, taken to be 24 nm. Suppose that s_{prd} is the predicted downrange distance by Eq. (22) with the current values of the nodes D_i^*. Then the drag profile update is done to each of the remaining node[2]

$$D_i = \frac{s_{prd}}{s_{to-go}} D_i^* \tag{27}$$

Given the piecewise linearity of the drag profile, this update is equivalent to scaling the entire

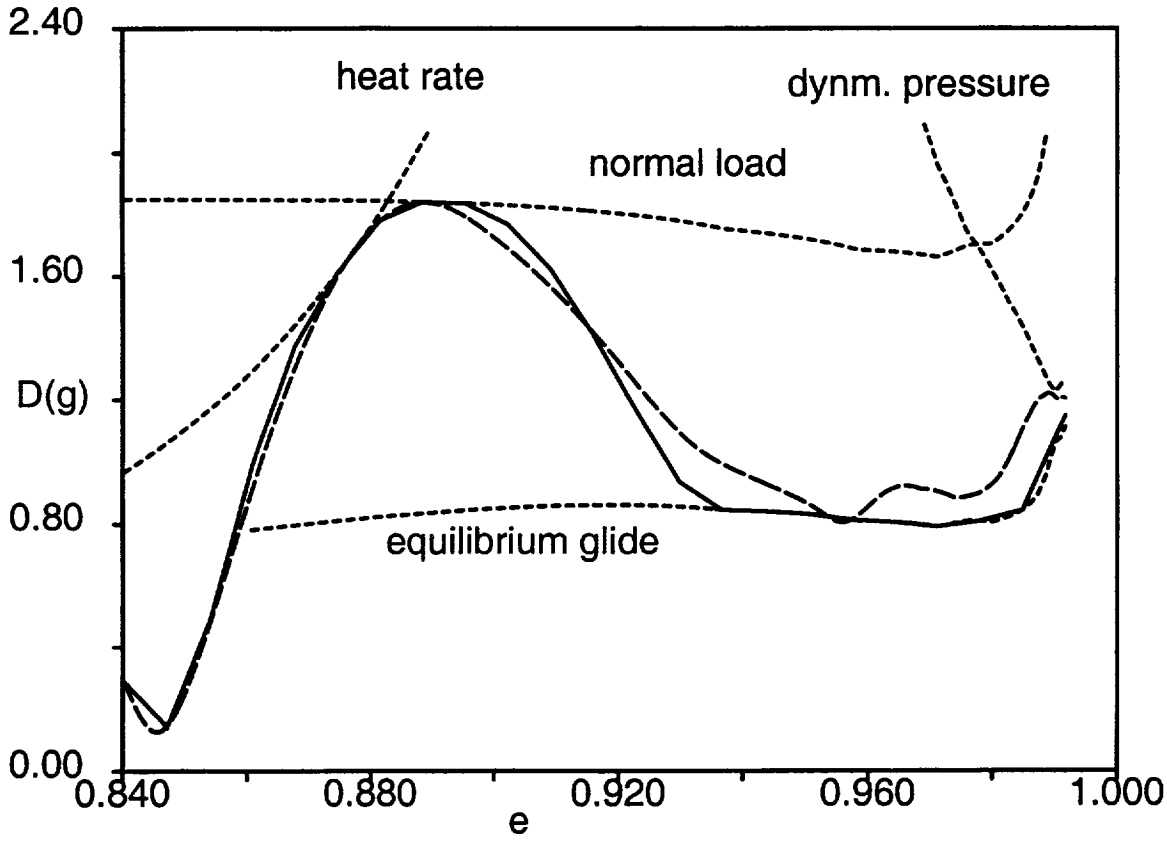

Figure 4: Comparison of drag profiles for landing at Malmstrom (solid-line: piecewise linear $D(e)$; dashed-line: along the trajectory in Fig. 3)

reference drag profile by a factor of s_{prd}/s_{to-go}, therefore the predicted downrange distance determined by the updated drag profile from Eq. (22) is now exactly s_{to-go}.

In addition to update (27), it is realized that the discrepancy in the initial energy level of the trajectory also contributes to range errors. Hence a one-time compensation to this effect is desired. At the initiation of the closed-loop guidance, let the actual energy level be e_0, and the nominal energy at the same point be e_0^*. Note that e_0 and e_0^* may be different because of the uncertainties and dispersions associated with the ascent. The final energy e_f is fixed. Thus the very first update should be

$$D_i = \left(\frac{s_{prd}}{s_{to-go}}\right)\left(\frac{e_f - e_0}{e_f - e_0^*}\right) D_i^* \tag{28}$$

This update procedure represented in Eqs. (27)-(28) is found to be one of the important factors that enhance noticeably the robustness of the performance of the entry guidance algorithms in the presence of significant trajectory dispersions. For the simulations reported in Section 7, the update is done once every second. It should be noted, though, that caution must be exercised when the reference drag profile lies close to the boundaries of the entry flight corridor specified by constraints (8-10). In such a case the scaling of the drag profile by (27) (or (28)) could result in the update drag profile violating some of these constraints.

Another updating scheme is described in Ref. [8] which updates the nearest few segments of the drag profile at a time. Suppose that at the instant of updating, the current energy e is between $[e_i, e_{i+1}]$, and that the difference between the range-to-go predicted by the analytical Eqs. (22) and (23) and the actual range-to-go is δs. To null the error δs the nodes D_{i+1},..., D_{i+k} are to be adjusted. Let the perturbations for the nodes be δD_{i+1}, ..., δD_{i+k}. The first-order expansion of the range-to-go is then

$$\delta s = \left(\frac{\partial \Delta s_i}{\partial D_{i+1}} + \frac{\partial \Delta s_{i+1}}{\partial D_{i+1}}\right)\delta D_{i+1} + \cdots + \left(\frac{\partial \Delta s_{i+k-1}}{\partial D_{i+k}} + \frac{\partial \Delta s_{i+k}}{\partial D_{i+k}}\right)\delta D_{i+k} \triangleq \mathbf{c}^T \delta \mathbf{D} \tag{29}$$

where all the partial derivatives are analytically evaluated, and $\delta \mathbf{D} = (\delta D_{i+1} ... \delta D_{i+k})^T$. The Eq. (29) admits infinitely many solutions when $k > 1$. But the minimum-norm solution, which is the one with the smallest $\|\delta \mathbf{D}\|^2 = \delta \mathbf{D}^T \delta \mathbf{D}$, is given by

$$\delta \mathbf{D} = \frac{\delta s}{\mathbf{c}^T \mathbf{c}} \mathbf{c} \tag{30}$$

The updated values of the nodes $D_{i+1}, ..., D_{i+k}$ are then given by $D_{i+1} + \delta D_{i+1}$, ..., and $D_{i+k} + \delta D_{i+k}$. The updated piecewise linear drag profile is thus obtained.

The effectiveness of the two approaches on improving the downrange distance accuracy is comparable to each other. Since the piecewise linearity of the reference drag profile renders the scaling of the entire drag profile no more difficult than adjusting a few segments at a time, the scaling approach is probably more preferable, although the second approach applies to any other analytical parametrizations of the drag profile.

4. Trajectory Control

While the design of drag profile is carried out off-line, trajectory control deals with on-board feedback tracking of the reference drag profile. Similar to the Shuttle, the X-33 will use both bank-angle and angle-of-attack modulations to control the entry trajectory, with bank angle as the primary long-period trajectory control and angle of attack as the fast trajectory shaping means.

4.1 Bank Angle Control Law

A nonlinear proportional-plus-integral-plus-derivative (PID) control law for the bank angle is used in this research. The control law is derived by using a nonlinear predictive control method.[8].

Denote $u = C_L \cos\sigma / C_D$, ignoring the rotation of the Earth, $\dot{C}_D$ and $\ddot{C}_D$, we can express

$$\ddot{D} = a_D + b_D u \tag{31}$$

where a_D and b_D are functions of r, V, γ and D, which can be readily obtained from the definition of D and Eqs. (1) and (4). Let $\Delta D = D - D^*$ with D^* representing the reference drag acceleration. Define an auxiliary variable

$$z(\tau) = \Delta\dot{D} + 2\zeta\omega_n \Delta D + \omega_n^2 \int_0^\tau \Delta D(\mu) d\mu \tag{32}$$

where $\zeta > 0$ and $\omega_n > 0$ are two constants. At any instant τ the influence of $u(\tau)$ on $z(\tau+T)$ for a time increment $T > 0$ can be predicted by a first-order Taylor series expansion

$$\begin{aligned} z(\tau+T) &\approx z(\tau) + T\dot{z}(\tau) = z(\tau) + T[a_D(\tau) \\ &+ b_D(\tau)u(\tau) + 2\zeta\omega_n \Delta\dot{D}(\tau) \\ &+ \omega_n^2 \Delta D(\tau) - \ddot{D}^*(\tau)] \end{aligned} \tag{33}$$

where for the piecewise linear parametrization of D^* with respect to e, we have in the interval $[e_i, e_{i+1}]$

$$\dot{D}^* = a_i DV, \quad \ddot{D}^* = a_i(\dot{D}V + D\dot{V}) \tag{34}$$

where a_i is from Eq. (17). Note that for accurate tracking of D^*, we desire that $z \to 0$. To find the control u for this purpose, consider the minimization of the performance index

$$J = \frac{1}{2} z^2(\tau + T) \tag{35}$$

at an arbitrary $\tau \in [0, \tau_f)$. Replacing $z(\tau+T)$ by Eq. (33) and setting $\partial J / \partial u(\tau) = 0$ give a continuous, nonlinear feedback control law

$$\begin{aligned} u(\tau) &= -\frac{1}{Tb_D}\Big[z + T(a_D - \ddot{D}^* + 2\zeta\omega_n \Delta\dot{D} \\ &+ \omega_n^2 \Delta D)\Big] \end{aligned} \tag{36}$$

This is a nonlinear PID control law when z is replaced by its definition (32). Globally asymptotically stable tracking of D^* for any $T > 0$ under this control law can be seen by substituting Eq. (36) into the equation for $\dot{z}$ to arrive at

$$\dot{z} = -\frac{1}{T}z \tag{37}$$

Thus $z \to 0$ exponentially with a time-constant T, and $\dot{z} \to 0$. From the definition of z, $\dot{z} = 0$ leads to

$$\Delta\ddot{D} + 2\zeta\omega_n\Delta\dot{D} + \omega_n^2\Delta D = 0 \tag{38}$$

Therefore, $\Delta D \to 0$ with a damping ratio of ζ and natural frequency of ω_n. For the X-33 applications, we have chosen $\zeta = 0.7$, $T = 0.01\sqrt{R_0/g_0}$ (sec), and $\omega_n = 0.04\sqrt{R_0/g_0}$, or $1/\omega_n$ corresponds to 25 sec in real time. The magnitude of the commanded bank angle σ_{com} for trajectory tracking is computed from $\cos\sigma_{com} = uC_D/C_L$.

A clear advantage of this predictive control method is that the 3rd-order closed-loop dynamics under the control law are decomposed into a simple fast-decaying first-order dynamics (37) and a well-understood 2nd-order steady-state dynamics (38). This decomposition allows convenient determination of the controller parameters T, ζ, and ω_n because they bear obvious physical meanings.

In the implementation, the computed σ_{com} is also constrained by the following amplitude, rate, and acceleration limits

$$\begin{aligned} &|\sigma_{com}| \le 85\ (deg), \quad |\dot{\sigma}_{com}| \le 5 - 10\ (deg/s), \\ &|\ddot{\sigma}_{com}| \le 2\ (deg/s^2) \end{aligned} \tag{39}$$

where the rate and acceleration are computed by finite differences.

The cross range is controlled by orientation of the bank angle. A simple dead-zone criterion for reversing the sign of the bank angle, similar to the one employed by the Space Shuttle,[1] is used in this scheme. Suppose that ψ^* is the azimuth pointing from the current position toward the center of the HAC. When the magnitude of the azimuth error $|\psi - \psi^*|$ exceeds a dead-band limit of 10 deg, the bank angle is reversed to the opposite direction. Note that due to the rate constraint in Eq. (39), the bank reversals cannot be achieved instantaneously.

4.2 Angle of Attack Modulation

The nominal angle of attack is scheduled with respect to Mach number. In many cases it is found that relying on bank angle modulation as described above is adequate to track the reference drag profile for the X-33. But in other more demanding cases such the maximum delay-to-transition-to-turbulence mission (dubbed as the "d" trajectory), where a long open-loop transition phase exists (up to 85 seconds) before closed-loop entry guidance, modulation in α can make a dramatic difference in guidance performance. A simple static, first-order α-modulation is used when necessary. Treat the drag acceleration as a *static* function of α and expand the drag with an anticipated increment $\Delta\alpha$ by

$$D(\alpha + \Delta\alpha) = D(\alpha) + \frac{\partial D}{\partial \alpha}\Delta\alpha \tag{40}$$

where α is the current sensed angle of attack. Let e be the current energy level. Set $D(\alpha + \Delta\alpha) = D^*(e)$. Then the above equation gives the required $\Delta\alpha$, thus

$$\alpha_{cmd} = \alpha + \Delta\alpha = \alpha + \left(\frac{\partial D}{\partial \alpha}\right)^{-1} (D^* - D) \tag{41}$$

and α_{cmd} is used as the angle of attack guidance command, subject to magnitude ($|\alpha_{cmd}| \leq \alpha_{nominal} + 5°$), rate, and acceleration constraints.

It should be noted that the above α-modulation ignores the dynamic effects on the drag. Yet it already proves to be a quite effective way of reducing trajectory dispersions in difficult situations. When this modulation was used in simulation results shown in this report, it will be so stated (section 6.2).

5. Pre-TAEM Lateral Trajectory Control

When the vehicle reaches the TAEM point by following the designed drag profile, bank reversals cannot ensure the strict alignment of the heading angle to the HAC or satisfaction any other specified requirements in heading. The final heading can be far from the desired direction, especially when the vehicle is required to approach the TAEM point from a specified direction which is not "natural" to the entry trajectory. For instance, the entry flight of the X-33 is from southwest to northeast (cf. Fig. 2), but in an early mission design for landing at Malmstrom AFB the X-33 is required to approach the TAEM point *from* southeast to avoid flight over the city of Great Falls. Even in the absence of such stringent requirement, the X-33 would not have enough time to correct the trajectory if the velocity heading at the TAEM interface is not pointed toward the HAC tangency.

Figures 5–7 show the TAEM conditions of 100 X-33 trajectories in Monte Carlo simulation for landing at Michael AAF. The trajectory dispersions are caused by uncertainties in propulsion system propellant loading, aerodynamics and navigation, all described in Section 6. The entry flight is guided entirely by the drag-tracking approach. At TAEM, the nominal altitude is 825,000ft, and the nominal downrange distance to HAC is 19 nm. Figures 5 and 6 show that while the longitudinal trajectory is controlled satisfactorily with the dispersions in TAEM altitude less than the $\pm$5000 ft specification, and the downrange distance dispersions less than the $\pm$5 nm specification, the heading errors are unacceptable. The mean heading error is about 15 deg, with some as large as 25 deg. Figure 7 reveals that despite the tight angle of attack α dispersions around the nominal value of 15 deg, the bank angle at TAEM is almost evenly distributed between $\pm$85 deg. Large bank angles at TAEM interface are the result of large heading errors at TAEM, and are not desirable because the subsequent TAEM trajectory control will be adversely affected.

There are two major contributing factors to the phenomena observed in Figs. 5–7: (1) in general the heading error will continue to increase for some time due to the fact that bank angle cannot instantaneously reverse to the opposite side after the bank angle command is reversed when the heading error exceeds the threshold value; (2) when the vehicle gets close to the HAC, the variation of the azimuth ψ^* to the HAC becomes faster. Consequently a bank reversal is always called for near the TAEM interface. But the bank rate

and acceleration constraints in Eq. (39) severely limit the speed of the bank reversal, thus resulting large overshoot of the heading error at the TAEM interface. Using a smaller heading error threshold value for bank reversals does not seem to solve this problem effectively, but increases the number of bank reversals unnecessarily. This challenge necessitates the use of a different guidance strategy before the vehicle reaches the TAEM interface. Two different methods are discussed below. The vehicle is under the drag-tracking guidance until it reaches a distance before the TAEM point. From this point to TAEM, one of the next two guidance logics is applied.

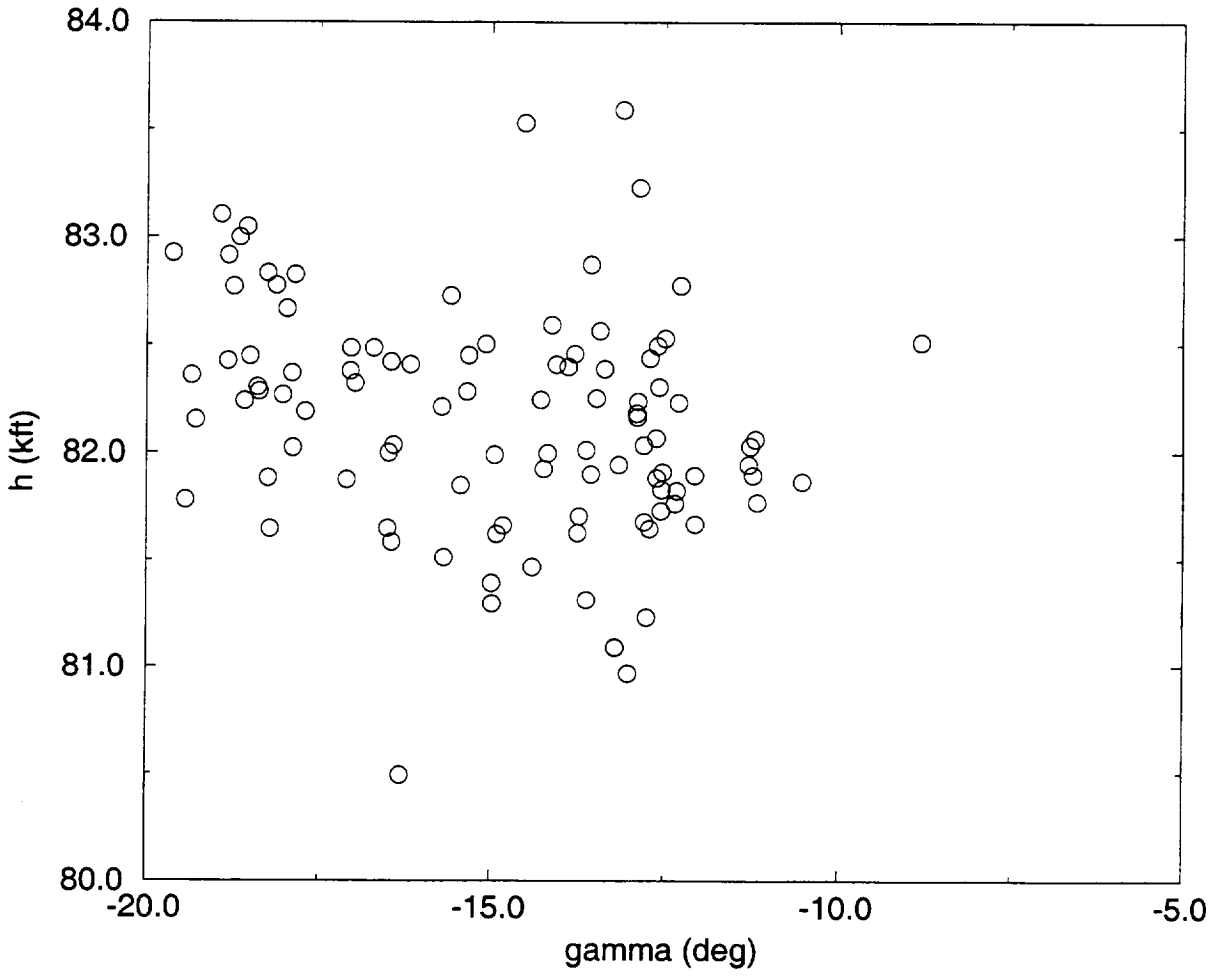

Fig. 5: Altitude and flight path angle at TAEM interface without heading control

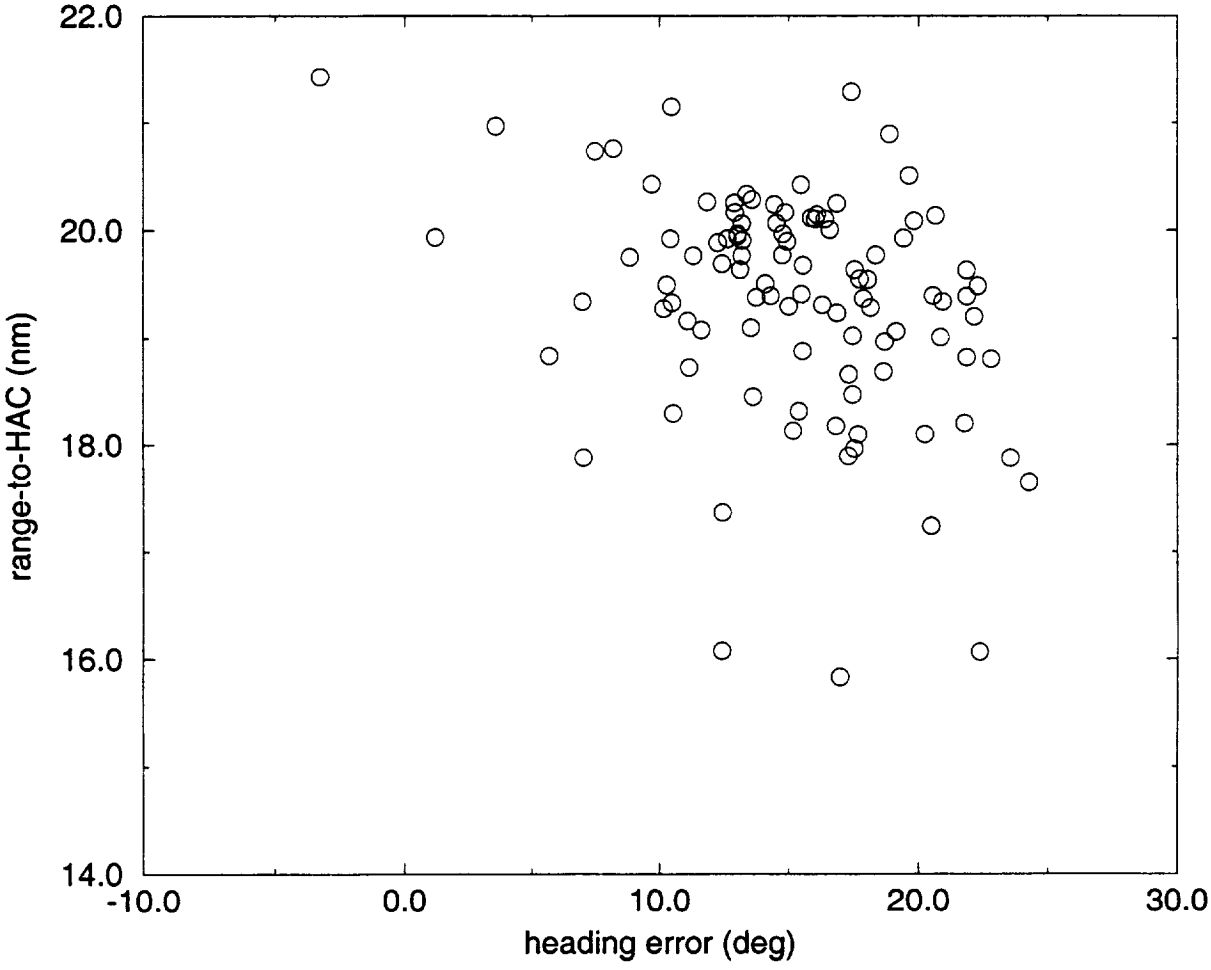

Fig. 6: Heading-to-HAC error and range-to-HAC at TAEM interface without heading control

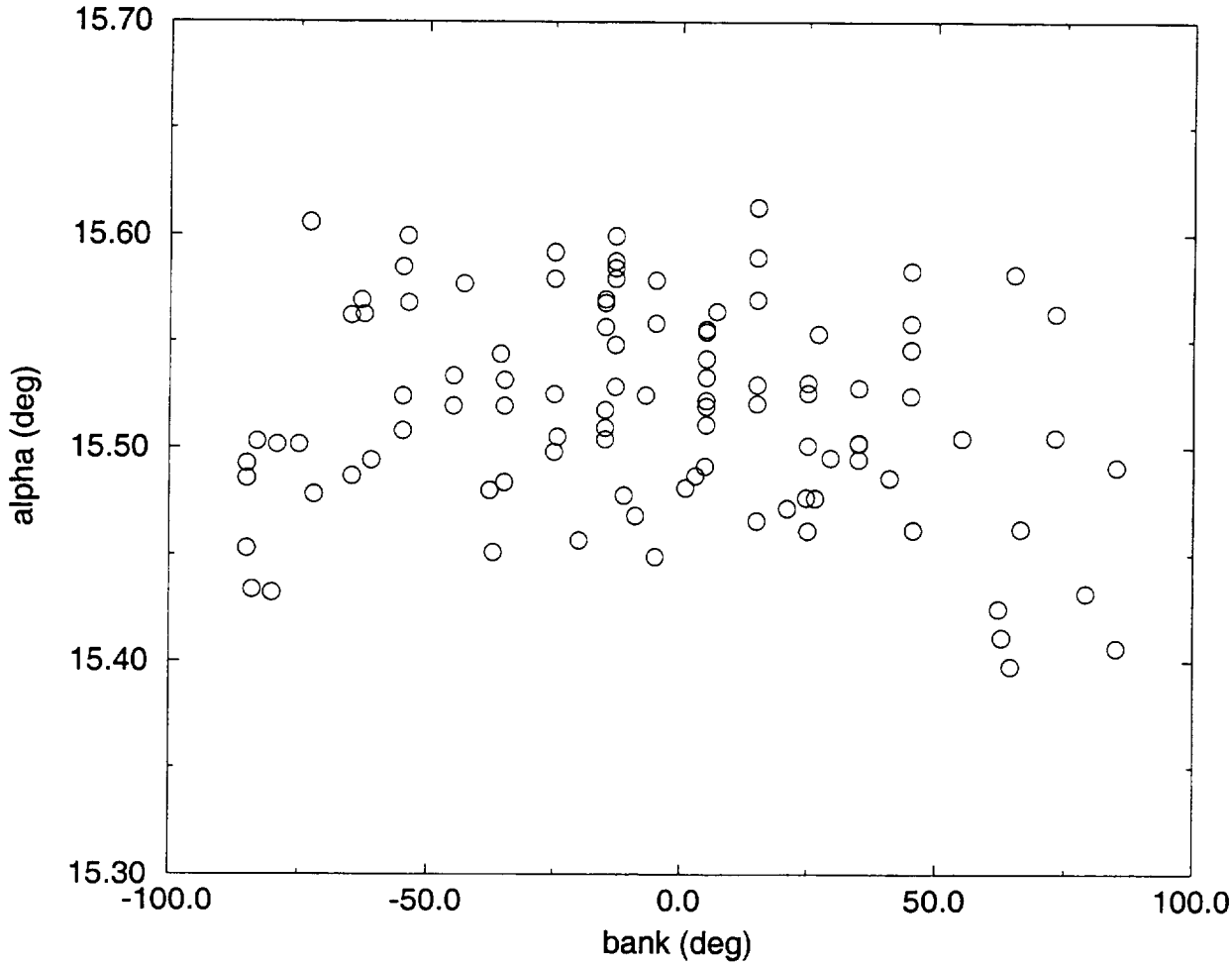

Fig. 7: Bank angle and angle of attack at TAEM interface without heading control

5.1 Ground-Track Control

In this approach we assume that a specific point at a nominal distance from the HAC is chosen to be the TAEM point. The heading angle at this point is also required to have a given value ψ_d. Use flat earth assumption in this phase. Let oxy be a coordinate system centered at the TAEM point with the y-axis pointing to the North, and x-axis to the East, as shown in Fig. 8. The kinematics of the vehicle in the horizontal plane are

$$\dot{x} = V\cos\gamma\sin\psi \tag{42}$$

$$\dot{y} = V\cos\gamma\cos\psi \tag{43}$$

From these two equations we have

$$\frac{dx}{dy} = \tan\psi \tag{44}$$

The desired ground track is chosen to be a cubic curve

$$x = ay^3 + by^2 + cy \tag{45}$$

where the coefficients a, b and c are to be determined. Suppose that at the instant τ_0 when the tracking of the ground track begins, $x(\tau_0) = x_0$ and $y(\tau_0) = y_0$, and the line-of-sight angle from the vehicle to the TAEM point is ψ_0^*. Let the azimuth (heading) angle required at the TAEM interface be denoted by ψ_d. First we set $c = \tan\psi_d$. Then along Eq. (45) at the TAEM point where $x = y = 0$,

$$\frac{dx}{dy}|_{x=y=0} = \tan\psi(\tau_f) = c = \tan\psi_d \tag{46}$$

Thus $\psi(\tau_f) = \psi_d$. The coefficients a and b are found by satisfying

$$x_0 = ay_0^3 + by_0^2 + cy_0 \tag{47}$$

$$\frac{dx}{dy}|_{\tau=\tau_0} = 3ay_0^2 + 2by_0 + c = \tan\psi_0^* \tag{48}$$

The condition Eq. (47) means that the desired ground track Eq. (45) starts at the current point; Eq. (48) specifies that the ground track directly points toward the TAEM point (origin) at the beginning. This condition is found important because with Eq. (48) the desired ground track conforms with the general direction of motion of the vehicle, thus the ground track is achievable by the vehicle. The solution to these two equations is

$$a = -[2(x_0 - y_0\tan\psi_d) - y_0(\tan\psi_0^* - \tan\psi_d)]/y_0^3 \tag{49}$$

$$b = [3(x_0 - y_0\tan\psi_d) - y_0(\tan\psi_0^* - \tan\psi_d)]/y_0^2 \tag{50}$$

Now, by following the ground track Eq. (45) with the coefficients defined in Eqs. (46), (49) and (50), the vehicle will reach the TAEM point at $x = y = 0$ with $\psi(\tau_f) = \psi_d$. This ground track can be easily designed on-board, given the navigation information on x_0, y_0 and ψ_0^*.

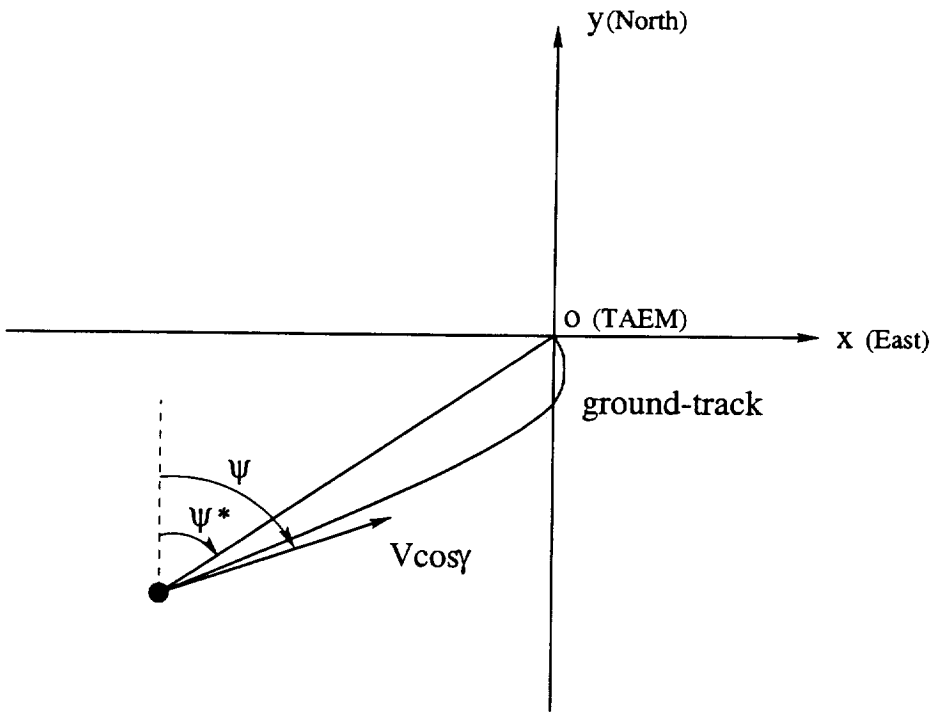

Fig. 8: Coordinate system for the final ground-track planning

Next, we will derive the bank-angle control law to track Eq. (45). To avoid differentiation of γ, which involves the term $\cos\sigma$, thus makes it difficult to obtain a closed-form control law, we introduce a new independent variable ξ

$$\xi = \int_{\tau_0}^{\tau} V(\nu)\cos\gamma(\nu)d\nu \tag{51}$$

or,

$$d\xi = V\cos\gamma d\tau \tag{52}$$

Therefore the kinematic Eqs. (42) and (43) become

$$x' = \sin\psi \tag{53}$$

$$y' = \cos\psi \tag{54}$$

where the prime stands for differentiation with respect to ξ. Let

$$F = x - ay^3 - by^2 - cy \tag{55}$$

Thus

$$F' = \sin\psi - 3ay^2\cos\psi - 2by\cos\psi - c\cos\psi \tag{56}$$

$$F'' = [\cos\psi + (3ay^2 + 2by + c)\sin\psi]\psi' - (6ay + 2b)\cos^2\psi \triangleq A_F\psi' + B_F \tag{57}$$

where from Eq. (6) with the Earth's rotation ignored, and Eq. (52), we have

$$\psi' = \dot{\psi}/V\cos\gamma = (L/V^2\cos^2\gamma)\sin\sigma + V\sin\psi\tan\phi/r \triangleq G_\psi\sin\sigma + H_\psi \tag{58}$$

Choose a feedback linearization control law

$$\sin\sigma = (-A_F H_\psi - B_F - 2\zeta_F \omega_{n_F} F' - \omega_{n_F}^2 F)/A_F G_\psi \tag{59}$$

where $\zeta_F > 0$ and $\omega_{n_F} > 0$ are two constants. Substituting Eqs. (58) and (59) into Eq. (57) gives the closed-loop dynamics

$$F'' + 2\zeta_F \omega_{n_F} F' + \omega_{n_F}^2 F = 0 \tag{60}$$

It follows that $F \to 0$, or $x = ay^3 + by^2 + cy$, asymptotically.
Remarks:

1. The new variable ξ is introduced only to enable us to derive the closed-form control law. The control law Eq. (59) is a function of the position coordinates and other states, independent of ξ.

2. It should be noted that ω_{n_F} is the natural frequency in ξ, not in the real time t or dimensionless time τ. So the value of ω_{n_F} may not have exactly the same influence on the transient tracking response in the real time, but it should still have qualitatively similar effects. The steady-state response $F = 0$ is the same, which is what we desire.

3. The guidelines for selecting ω_{n_F} and, to a lesser extent, ζ_F, are such that: (1) the control law Eq. (59) is not severely saturated; and (2) the vehicle reaches the TAEM point with an acceptable energy level. For the entry flight of the X-33 to Malmstrom AFB tested in Section 5, we have used $\zeta_F = 0.7$ and $\omega_{n_F} = 350$, which corresponds to a dimensional natural frequency of $350/\sqrt{R_0/g_0} = 0.434$ (1/sec).

4. The starting point of the ground-track control phase may differ, depending on how hard the vehicle needs to maneuver to meet the final heading condition. In general, it should be initiated as close to TAEM as possible to ensure that the vehicle reaches TAEM with proper energy. For the X-33 landing at Malmstrom AFB, the difference between the required azimuth angle and the "natural" one is over 40 deg in our simulations. Hence the ground-track control is initiated at a distance of 150 km (at about Mach 5.2) from the TAEM interface to allow enough time for the maneuver.

5. When the ground track Eq. (45) is followed, the vehicle is guaranteed within the accuracy of the analysis to reach the TAEM point because the ground track Eq. (45) passes through the TAEM point, no matter whether or not there is a range error at τ_0. Therefore this feature is expected to improve the overall performance of the guidance algorithm in trajectory dispersion study. When the final ground-track control is employed, the updating of the drag profile discussed previously serves more the purpose of keeping the trajectory at correct energy level than eliminating the range error. See the discussion of the numerical results in Simulation section.

6. Even when the final heading of the entry trajectory is not required to meet a strict condition, the ground-track control can still be employed to achieve precise TAEM point location. In this case, ψ_d can be simply set to be equal to ψ_0^*. Then $a = b = 0$ by

Table 1: Comparison of TAEM conditions for landing at Malmstrom AFB

	d_f (km)	h_f (km)	V_f (m/s)	ψ_f (deg)	γ_f (deg)
Traj. 1	0	24.75	740.00	−5.14	−11.0
Traj. 2	47.57	24.70	739.90	−2.34	−16.3
Traj. 3	1.86	24.66	740.65	36.63	−14.6
Traj. 4	0.18	25.52	730.0	−5.75	−8.6

Eqs. (49) and (50), and the reference ground track Eq. (45) degenerates to a straight line. The vehicle will follow this straight line to the TAEM point. This usually is a much less aggressive maneuver for the vehicle compared to the case where a specified final heading is required.

While the control law Eq. (59) controls the lateral motion of the vehicle, the longitudinal motion needs to be monitored so that the trajectory constraints (8–10) will not be violated. Among them, constraint (9) $\bar{q} \leq \bar{q}_{max}$ is the predominant one (cf. Fig. 4) in this phase. To prevent the trajectory from descending too fast to violate (9), the angle of attack α is modulated in this period according to

$$\alpha = \alpha_{ref} + \alpha_q e^{-k_q(1-\bar{q}/\bar{q}_{max})} \tag{61}$$

where $\alpha_q > 0$ and $k_q > 0$ are two selected constants. Appropriate values for α_q and k_q will result in $\alpha \approx \alpha_{ref}$ when $\bar{q}$ is away from and less than $\bar{q}_{max}$, and α will increase as $\bar{q} \to \bar{q}_{max}$. As a result, the altitude decrease will slow down and $\bar{q} < \bar{q}_{max}$ will remain enforced. For our X-33 applications, $\alpha_q = 10$ deg and $k_q = 10$, among many other possible combinations, appear to work well.

The above scheme is applied in simulation to a Mach 14 trajectory for landing at Malmstrom AFB. Four different trajectories are given for comparison:

- Trajectory 1: obtained by trajectory optimization described in Section 2. This trajectory serves as the nominal the other trajectories will compare with.
- Trajectory 2: guided entirely by the drag-tracking method in Section 3, but without drag-profile update described in Section 3.2.
- Trajectory 3: similar to Trajectory 3, but with drag-profile update.
- Trajectory 4: guided by the drag-tracking guidance (including drag-update) till 150 km from the TAEM point, and then guided by the ground-track control scheme discussed above.

Table 1 lists the TAEM conditions along these four trajectories. The quantity d_f in Table 1 stands for the distance to the given TAEM point at the end of the trajectory h_f the TAME altitude, V_f the TAEM velocity, ψ_f the TAME velocity heading, and γ_f the TAEM flight path angle.

Figure 9 contains the nominal drag profile, and the drag profiles along Trajectory 2 and 3. While the trajectory control law (36) tracks the reference drag profile closely, without drag updating the trajectory misses the TAEM point by $d_f = 47.6$ km (Table 1). With drag updating, the miss-distance is reduced to only 1.86 km (Traj. 3). But the problem now is with the final azimuth angle ψ_f which is 36.6 deg, far from the required -5.14 deg. Adding the ground-track control phase previously developed effectively corrects this problem and further reduces the miss distance, yielding $\psi_f = -5.75$ deg and $d_f = 0.18$ km (Traj. 4).

Figures 10–11 compare the bank angle and angle of attack histories along Trajectory 3 and 4. The difference in the bank angle is only in the last 100 seconds or so when the ground-track control is applied. In Fig. 11 the visible small hump near the end of Traj. 4 is due to the angle of attack modulation, Eq. (61), when the trajectory moves closer to the boundary of $\bar{q} \leq \bar{q}_{max}$. Figure 12 shows the trajectory of Traj. 4 in solid-line in the velocity-altitude space with the constraint boundaries of Eqs. (8-11). Clearly all the constraints are met and the trajectory looks similar to Traj. 1, which is plotted in Fig. 3 in solid line. Without the angle of attack modulation Eq. (61), the constraint $\bar{q} \leq \bar{q}_{max}$ would have been violated in this case. Plotted in Fig. 13 are the ground tracks along Traj. 4 and 1. The ground-track control scheme ensures the satisfaction of the stringent heading requirement at the TAEM, and the ground track is virtually the same as that along the open-loop trajectory in Fig. 2.

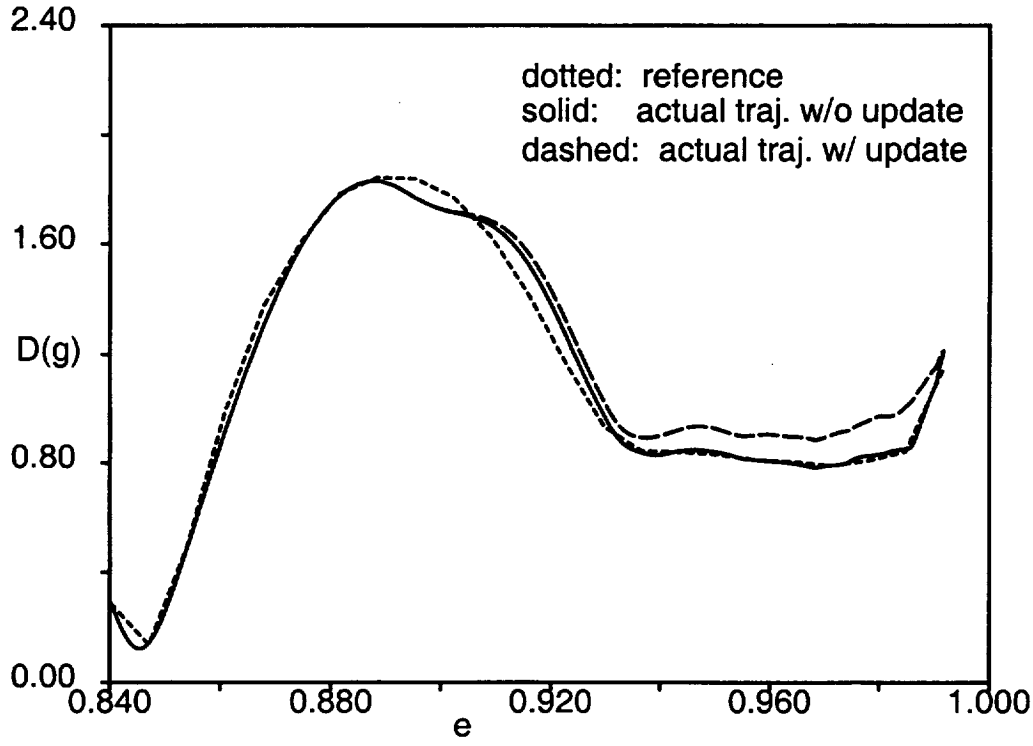

Fig. 9: Comparison of drag profiles for landing at Malmstrom with and without drag profile update

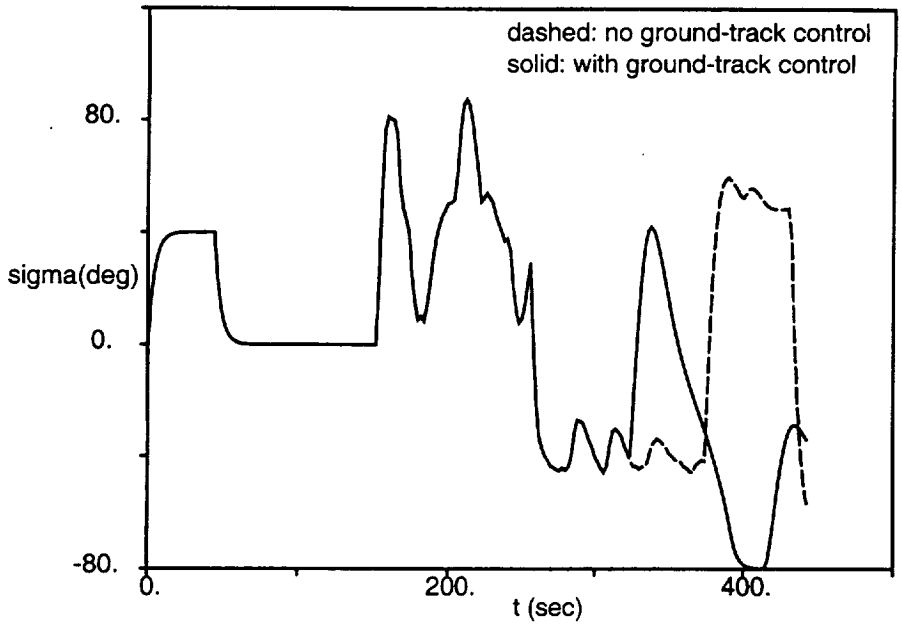

Fig. 10: Bank angle histories for the X-33 landing at Malmstrom

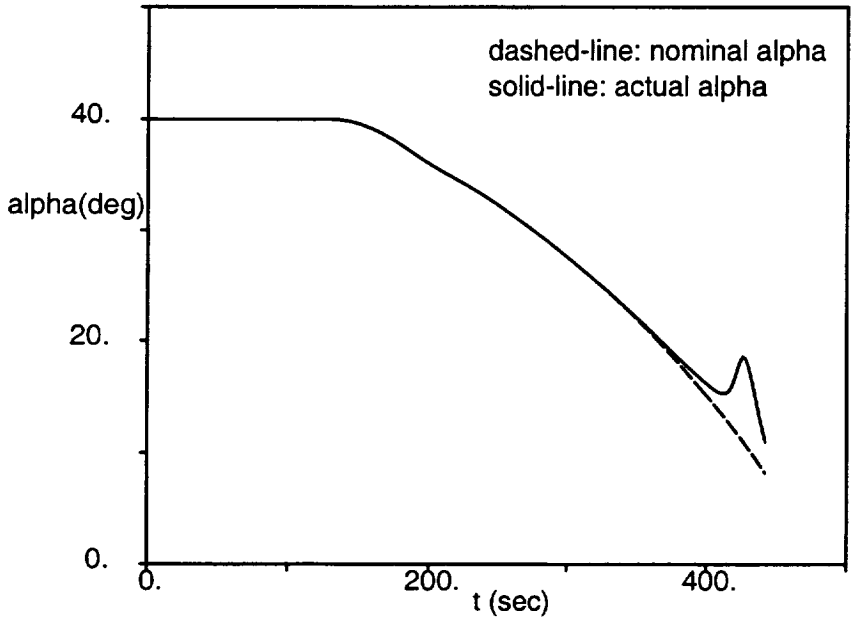

Fig. 11: Angle of attack of the X-33 landing at Malmstrom

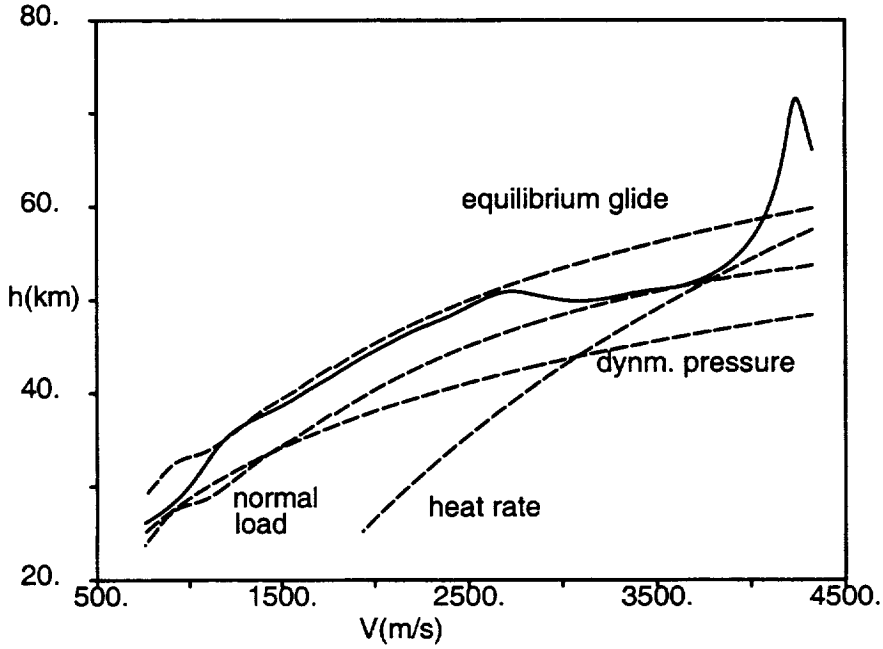

Fig. 12: Entry trajectory to Malmstrom generated by tracking the piecewise linear drag profile and controlling the pre-TAEM ground track

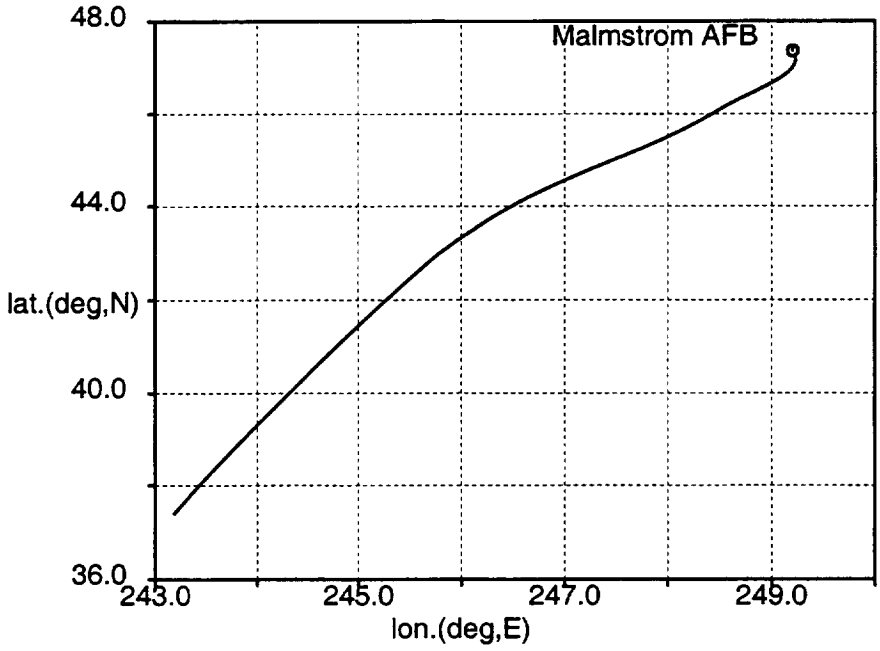

Fig. 13: Ground track of the X-33 landing at Malmstrom

5.2 Heading-Control by Proportional-Navigation Guidance

In this setting, we assume that the TAEM interface is not defined by a specific point (as opposed to the previous section where the TAEM interface is a well-defined point), instead by certain flight conditions (e.g., Mach 3.0 for the X-33). This is the case for the X-33 landing at Michael AAF in the final trajectory design. Upon arrival at the TAEM interface (wherever the actual location happens to be), the heading of the vehicle is required to be pointing directly at the HAC tangency. A method that can be employed for heading alignment of the vehicle toward the HAC before the vehicle reaches the TAEM interface is proportional-navigation (PN) guidance.

Proportional-navigation guidance has been an extensively researched guidance method in the literature because of its simplicity and effectiveness. The applications have been mainly in short-range interception. In almost all the analytical investigations of the PN guidance, a key assumption is constant velocity for the interceptor. In a recent work[13], the PN guidance method is extended to intercept of a nonmoving target by an interceptor with arbitrary time-varying velocity. It has been shown that in such a scenario, any navigation constant of greater than one will lead to intercept, and any navigation constant of greater than two will result in the interceptor to directly head toward the target (direct collision course). These developments appear to fit the current situation perfectly well: the velocity of the X-33 cannot be regarded as constant; the target point (HAC) is nonmoving; and the heading of the X-33 needs to be pointed to the HAC.

Let ψ^* be the azimuth angle from the current position to the HAC tangency. Given the HAC tangency coordinates and the current vehicle position, ψ^* is determined on-board. The PN guidance law is then used to command the vehicle heading angle

$$\dot{\psi} = \lambda \dot{\psi}^* \tag{62}$$

where a navigation constant of $\lambda > 2$ should be chosen. If the self-rotation of the earth is ignored, the bank angle control law corresponding to (62) is obtained from Eq. (6)

$$\sin\sigma = (\lambda V \dot{\psi}^* - \frac{V^2}{r}\cos\gamma \sin\psi \tan\phi)\cos\gamma / L \tag{63}$$

The guidance algorithm is switched to this PN guidance law at a distance d_0 from the HAC. For instance, in an early design of the X-33 trajectory to Michael AAF, d_0 is selected to be 35 nm where the nominal velocity is about Mach 3.6. This gives a range of about 16 nm for the PN guidance to align the heading to the HAC before the X-33 reaches the TAEM interface which is about 19 nm from the HAC and at Mach 2.5 (The latest design puts the interface at Mach 3.0 and 30 nm from the HAC). The choice of d_0 (or any other initiation criteria) is a matter of balancing competing objectives: longer d_0 gives more time for the PN guidance to work, thus provides tighter heading control. But the resulting downrange distance dispersion at the TAEM interface may exceed the specification because the longitudinal (drag-tracking) guidance is disengaged earlier.

A relatively large navigation constant of

$$\lambda = 5$$

is used to quickly orient the heading to the HAC in this period. An added advantage of this approach is that once the vehicle is heading toward the HAC, no significant trajectory maneuvers are needed, thus the bank angle at the TAEM interface will be relatively small.

When the bank angle control is switched from drag-profile-tracking to heading control (63), the longitudinal motion tends to produce too shallow a trajectory at the TAEM interface with high altitude and small flight path angle.[2] To compensate for this undesirable dispersion from the required TAEM conditions, in the period when the heading control (63) is in effect, the angle of attack α is modulated according to

$$\alpha = \alpha_{ref} - 1.5(\gamma - \gamma^*) \tag{64}$$

where α_{ref} is the nominal value of the angle of attack, and γ^* is a constant value determined on-board as follows: Let h_0 be the altitude at the distance d_0 from the HAC (where the final heading control phase is initiated), h_{taem} the specified TAEM altitude (82,000 ft), and d_{hac} the nominal distance from the TAEM interface to the HAC (115,446 ft, or 19 nm). Then

$$\tan\gamma^* = \frac{h_0 - h_{taem}}{d_0 - d_{taem}} \tag{65}$$

Evidently, the meaning of γ^* is such that if the vehicle flies a constant flight-path-angle trajectory at $\gamma = \gamma^*$, it would reach the TAEM interface at the altitude of h_{taem}. Note that h_0 is different along different trajectories, thus γ^* should be determined on-board. The modulation of α is limited by the constraints

$$|\alpha - \alpha_{ref}| \leq 5\ (deg), \quad |\dot{\alpha}| \leq 5\ (deg/sec) \tag{66}$$

6. Trajectory Dispersion Study

The algorithms described in Sections 2–5 are implemented for the X-33 in Monte Carlo simulations for landing at Michael AAF. The vehicle trajectory simulation is performed by a computer program called Marshall Aerospace Vehicle Representation in C, developed at the NASA Marshall Space Flight Center. The trajectory simulation is from lift-off through entry. Because of the evolving nature of the X-33 mission designs and MAVERIC during time span of this this research from 1997 to 1999, two sets of dispersion studies were done with different versions of MAVERIC and nominal trajectory designs.

6.1 Mission 7c6

In this case the TAEM interface is defined by the value of the specific energy corresponding to an altitude of 82,000 ft and Mach 2.5 (consistent with early X-33 mission design). The algorithms developed in this research were incorporated into MAVERIC 3.0 for entry guidance. The ascent and transition guidance schemes are from NASA Marshall and are implemented in MAVERIC. The simulation terminates when the energy reaches this value. The entry guidance command update cycle is one second. Figures 14 and 15 show the closed-loop bank angle and angle of attack histories along a nominal maximum catalytic heating trajectory. The PN guidance is used for the final heading control which started at $t = 400$

seconds from lift-off (at Mach 3.6, about 35 nm from the HAC). At the end of the nominal entry trajectory, the distance to the HAC is 19.5 nm, the heading error to the HAC is 0.22 deg, the altitude is 84,641 ft and velocity 2426 ft/s.

To evaluate the performance of the entry guidance scheme in the presence of uncertainties in propulsion, atmospheric properties, winds, navigation and aerodynamics, Monte Carlo simulations were performed. The propulsion system uncertainties include up to $\pm 1\%$ in I_{sp} (specific impulse), $\pm 1\%$ in propellant utilization, 404.1 lbm in loaded LOX and 54.96 lbm in loaded LH2. The aerodynamic coefficient uncertainty model is based on comparison of predicted versus actual flight data from past lifting body programs. MAVERIC randomly generates the uncertainties in the specified ranges and the corresponding trajectory. Atmospheric uncertainties were not included because of a difficulty in incorporating an atmospheric model software into MAVERIC at Iowa State University. But tests at NASA Marshall indicated that for the X-33 atmospheric uncertainties only play a secondary role compared to propulsion and aerodynamic uncertainties.

The simulation results of the TAEM conditions along 120 dispersed trajectories are summarized in Figs. 16–19. Figure 16 illustrates the dispersions of heading error and range-to-HAC. In comparison to Fig. 6 it is evident that the PN guidance markably improves the heading-to-HAC accuracy. The majority of the trajectories had heading errors within ± 2 deg, and all but two trajectories met the ± 5 deg heading error specification. The range-to-HAC had somewhat larger dispersions as compared to Fig. 6. The average value of range-to-HAC is 19.636 nm with a standard deviation of 2.489 nm. The ± 5 nm error specification on the range-to-HAC is still satisfied by predominant majority of the trajectories.

Figure 17 shows the altitude and flight path angle conditions at the TAEM interface. The trajectories generally end higher than the nominal value with the altitude having an average value of 84,378 ft and a standard deviation of 1,117 ft. The altitude dispersions are larger than those shown in Fig. 5 where no final lateral trajectory control was used. Yet all trajectories met the $\pm 5,000$ ft altitude dispersion requirement.

Figure 18 depicts the bank angle and angle of attack at the TAEM interface. The α-modulation (64) in most cases reduces the angle of attack in an attempt to lower the altitude. Without the α-modulation (64), the trajectories would terminate at altitudes as high as 93,000 ft. Because the trajectories headed directly toward the HAC in a nearly straight line under the PN guidance law (62), as a result the bank angle was relatively small, mostly confined between ± 25 deg, which is in sharp contrast to Fig. 7.

Finally, Fig. 19 contains the final velocity and altitude information. The average value of the Mach number at the TAEM interface is 2.497, with a standard deviation of 0.02. A nice correlation between the altitude and velocity is evident: a lower TAEM altitude is compensated with a higher TAEM velocity, and vice versa.

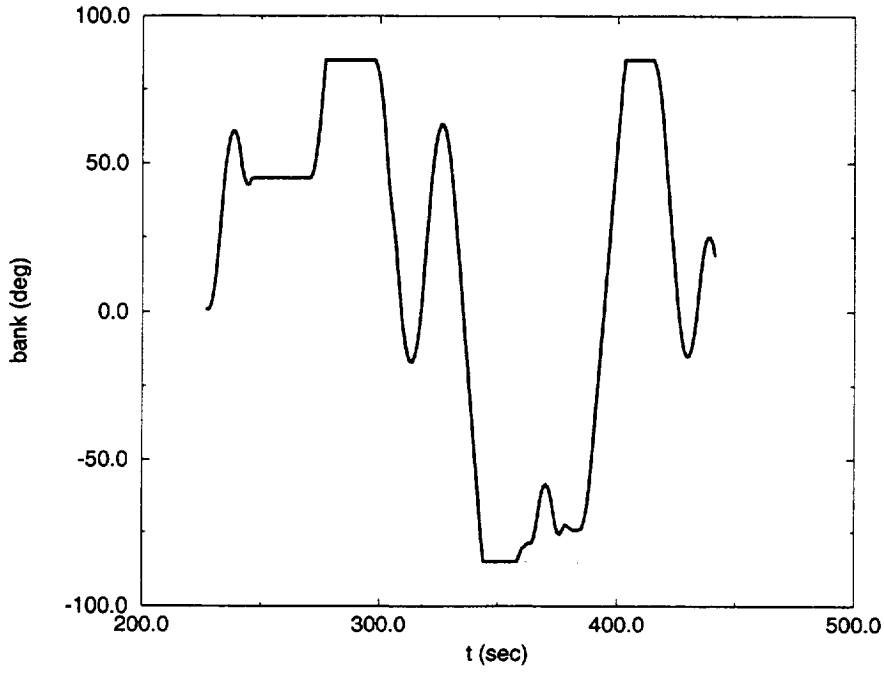

Fig. 14: Closed-loop bank angle history to Michael AAF

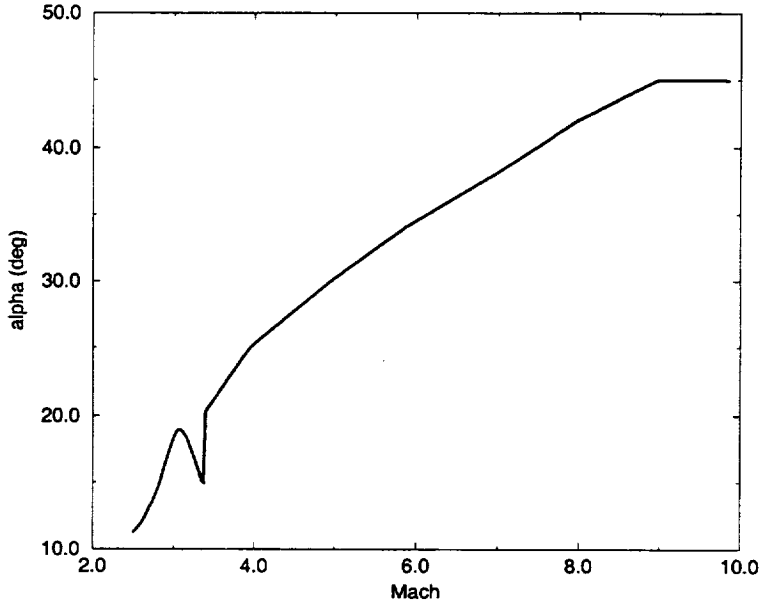

Fig. 15: Angle of attack history to Michael AAF

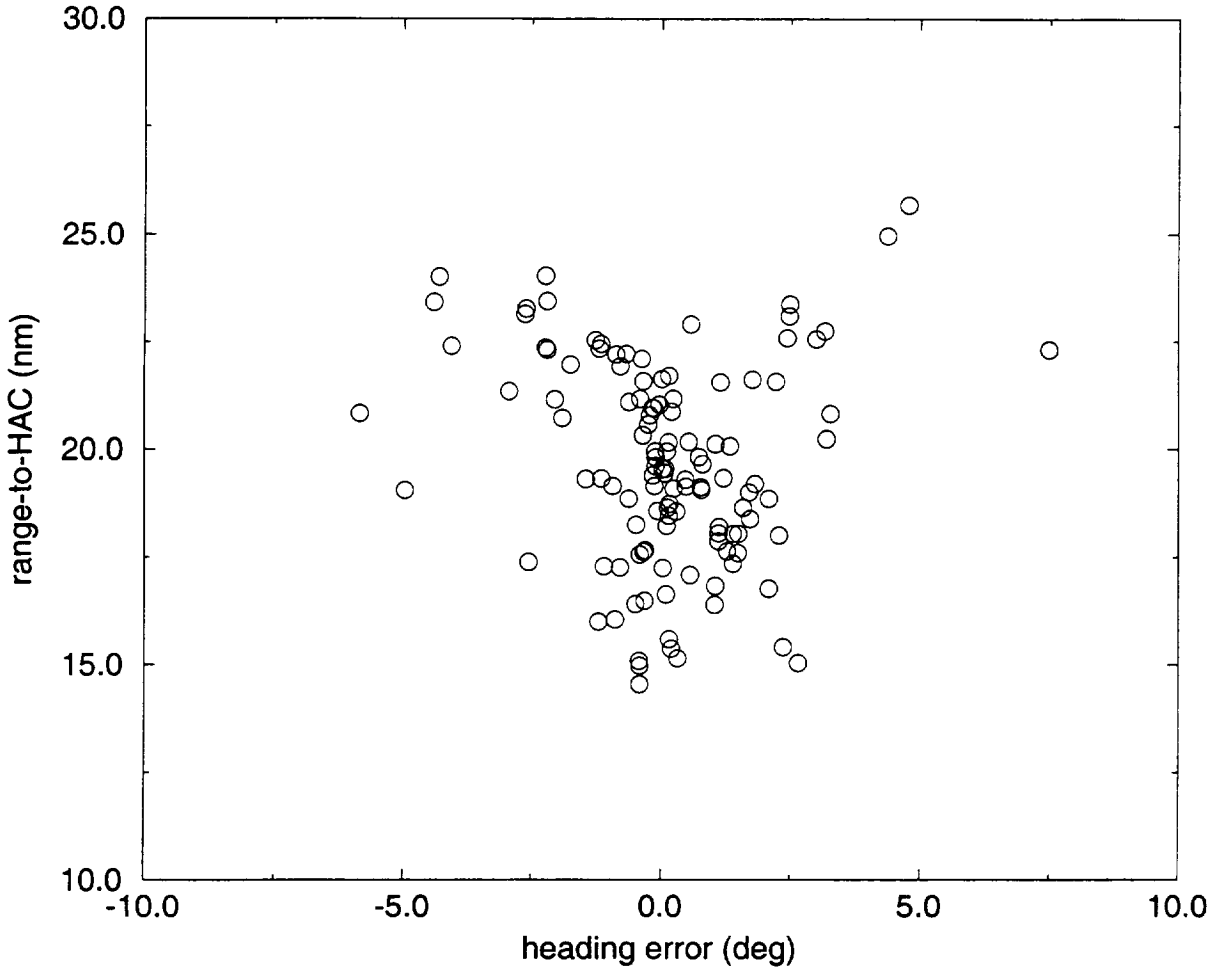

Fig. 16: Heading-to-HAC error and range-to-HAC at TAEM interface with heading control

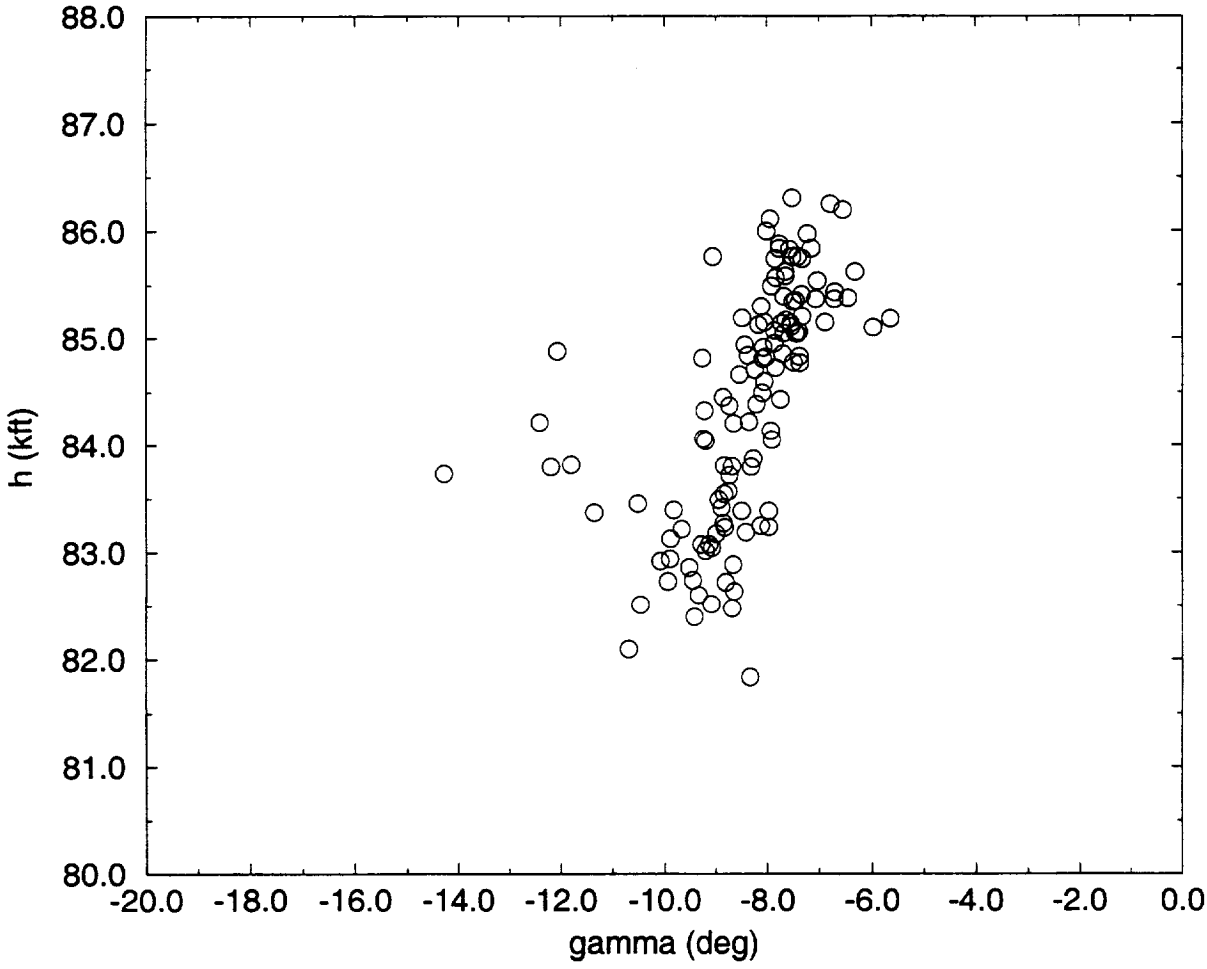

Fig. 17: Altitude and flight path angle at TAEM interface with heading control

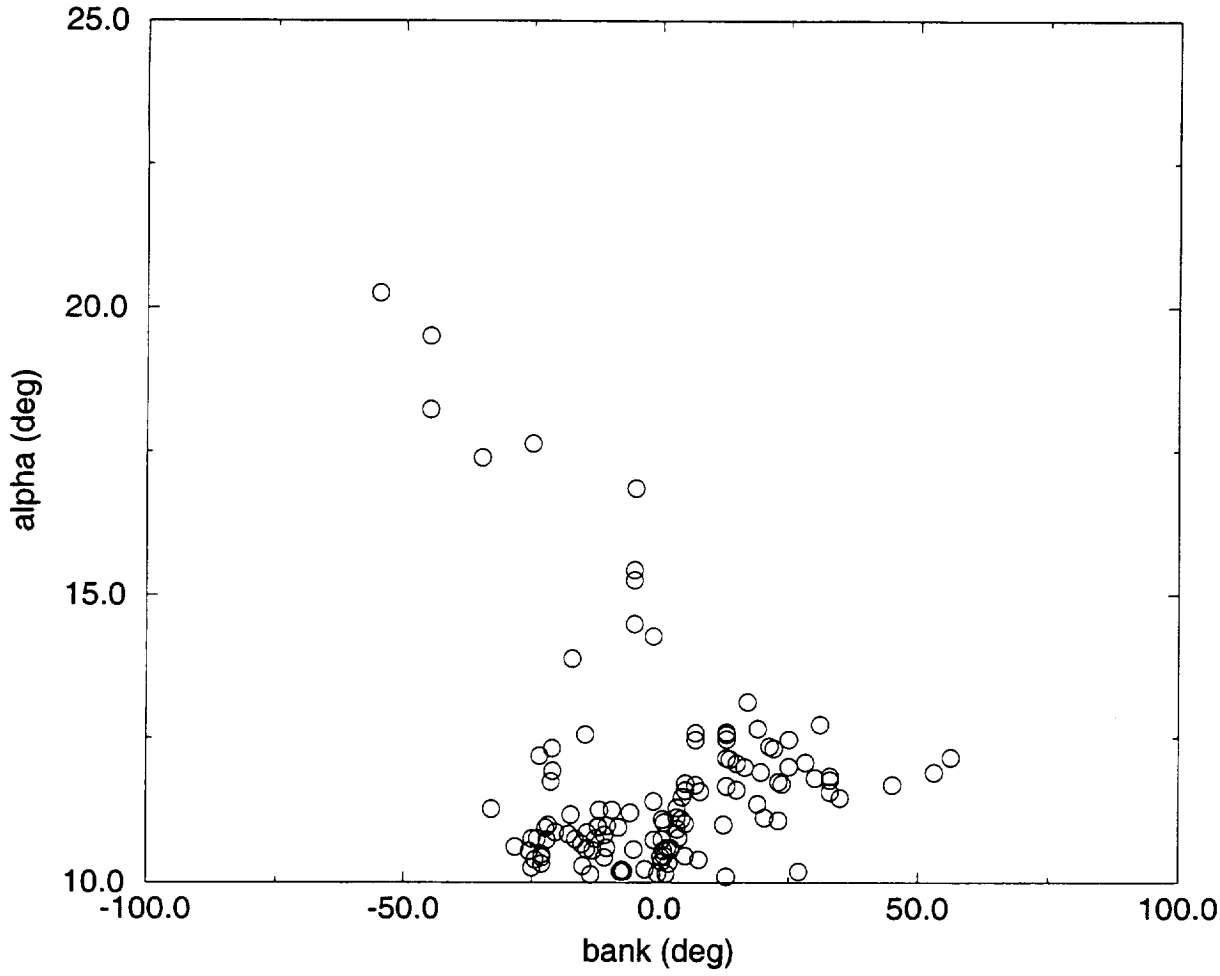

Fig. 18: Bank angle and angle of attack at TAEM interface with heading control

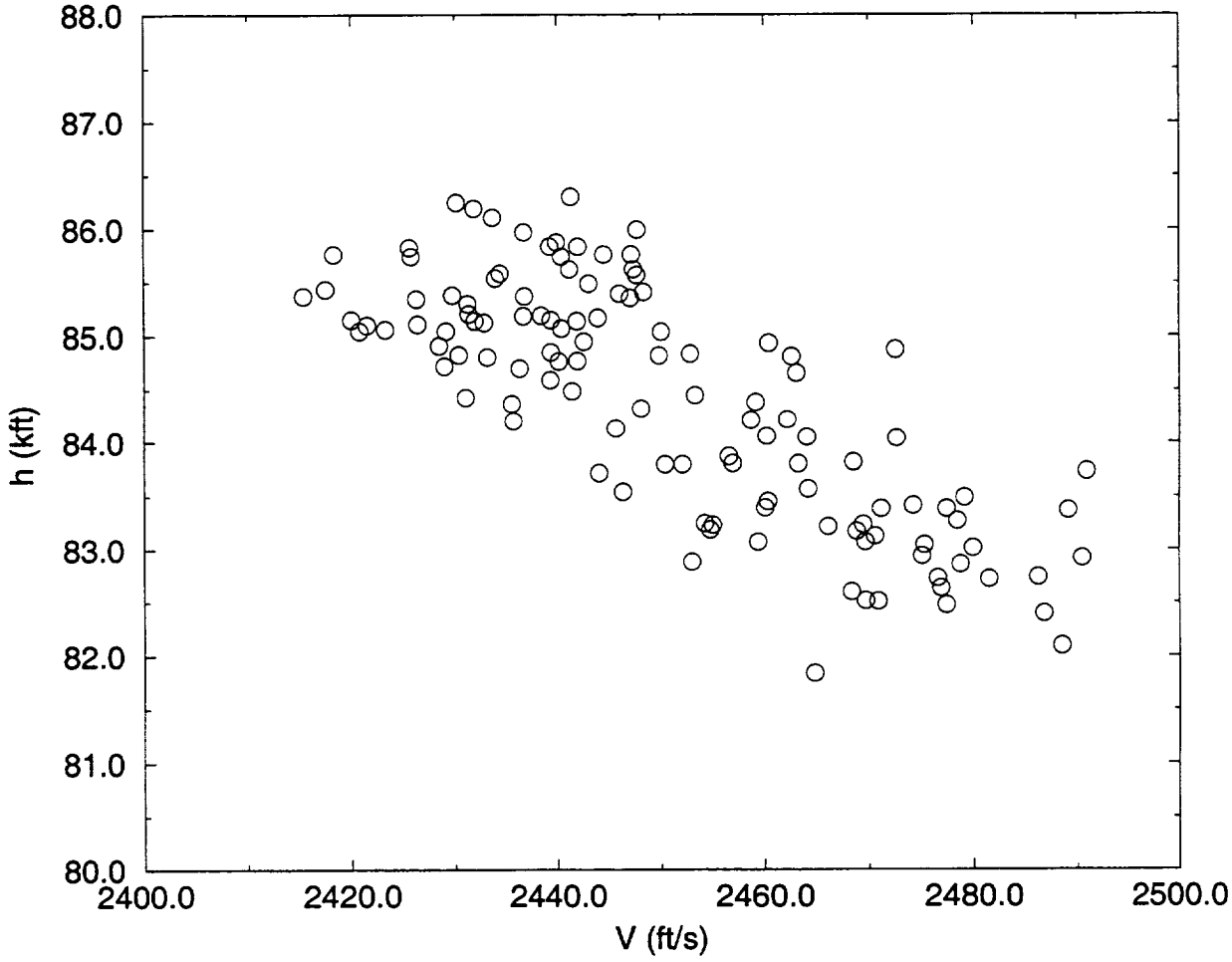

Fig. 19: Velocity and altitude at TAEM interface with heading control

6.2 Mission 9d5

This is a more recent study performed during the summer of 1999 [14]. The mission is designed to maximize the delay to transition-to-turbulence during entry flight to Michael AAF. Therefore there is a 85-second open-loop transition phase following MECO. This long transition phase reduces the period in which closed-loop entry guidance can correct the trajectory, and amplifies any trajectory dispersions occurred during the ascent. All these add to the difficulty in achieving tight control of trajectory dispersions. For the latest mission designs, the TAEM interface is defined at Mach 3.0, 30 nm from the HAC at 96,000 ft altitude (which further shortens the duration of entry guidance!). The dispersion study was performed with MAVERIC 6.7.2a against uncertainties in atmospheric parameters, winds, propulsion system, propellant utilization, interaction of jet effects with aerodynamics, aerodynamic

coefficients, and navigation data.

This mission is more difficult from entry guidance viewpoint. The α-modulation in Eq. (41) was found to be very useful in ensuring satisfactory guidance performance.[14] The performance is measured again by the dispersions in TAEM conditions. For comparison purpose, the X-33 entry guidance algorithms implemented in the MAVERIC was used to generate trajectories under the same uncertainties.

Figures 20–22 show the TAEM conditions along 150 dispersed trajectories under the entry guidance algorithms developed in this research at Iowa State University (ISU) and the actual X-33 entry guidance designed at Marshall Space Flight Center (MSFC). A downrange bias of 10 nm was set in the X-33 entry guidance I-loads to avoid too close a distance to HAC at the TAEM along few of the trajectories. It is clearly seen that the guidance schemes developed in this research was able to provide satisfactory performance even in this challenging case. The dispersions in the downrange distances to the HAC are within ± 5 nm; the heading angle errors less than 2.5 degrees; the altitude dispersions less than 4000 ft. Six degree-of-freedom simulations with MAVERIC have verified successful landing of the X-33 at the runway at Michael AAF for all the cases that had largest dispersions at the TAEM interface.

6.3 High Downrange Trajectory Sensitivity

During the course of this research it was discovered that under the current entry guidance framework, the downrange distance at TAEM can vary significantly with slight differences between to otherwise the same trajectories. Figure 23 illustrate this point: the downrange distances to HAC along 50 dispersed trajectory pairs under X-33 entry guidance algorithms (mission 9d5) are shown. The only difference between the two trajectories in each pair is slightly different navigation models implemented in MAVERIC. Yet at the TAEM interface the distances to HAC differ as large as 14 nm (e.g., cases 3,15, 45). Similar trend can be observed in Fig. 24 where the same 50 pairs of trajectories were simulated under the entry guidance algorithms developed in this project, although the differences were not as large. This high sensitivity was attributed to the pre-TAEM phase guidance where the heading control is emphasized, and both the X-33 entry guidance and the ISU guidance algorithms have such a phase which is a necessary for the X-33. In this phase, the longitudinal motion (downrange distance and altitude) is not tightly controlled because of the decoupled guidance strategy. As a consequence, small dispersions could result in significant differences in the longitudinal direction as observed. Indeed, if the pre-TAEM phase is removed, the same 50 pairs of trajectories will all have range-to-HAC at near 30 nm (the nominal value) as demonstrated in Fig. 25. Note how accurately the downrange distance is controlled by the entry guidance algorithms despite the considerable uncertainties introduced in the Monte Carlo simulations. However, the heading angle errors (not shown) along those 50 pairs of trajectories at TAEM are as large as 20 degrees, which is not acceptable for the X-33.

This trade off between longitudinal and lateral guidance precision is inherited in the current decoupled framework of entry guidance methods, and cannot be eliminated as long as there are competing requirements in lateral direction that need to be met.

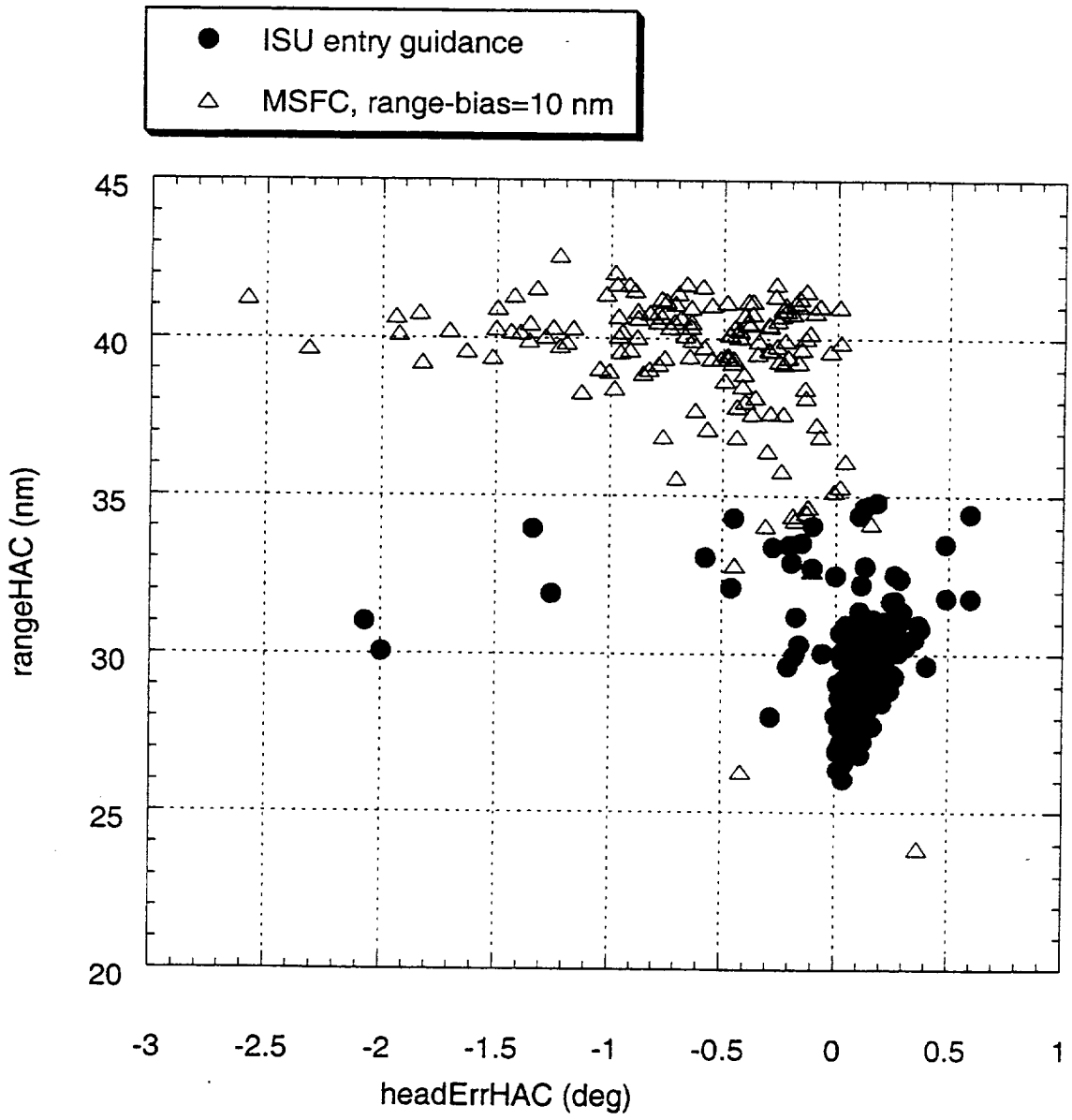

Fig. 20 Heading error and range-to-HAC at TAEM for 150 dispersed trajectories

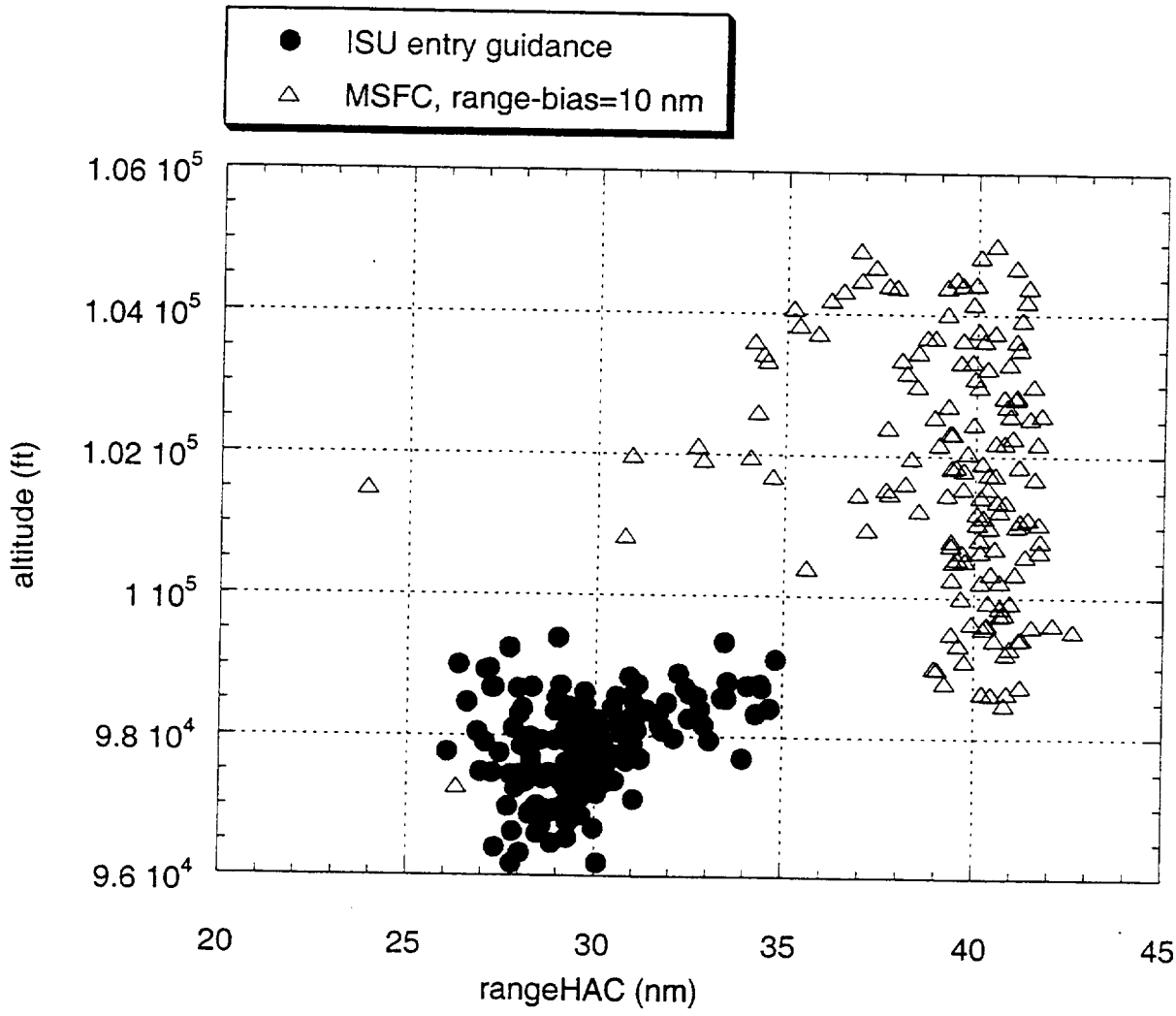

Fig. 21 Range-to-HAC and altitude at TAEM for 150 dispersed trajectories

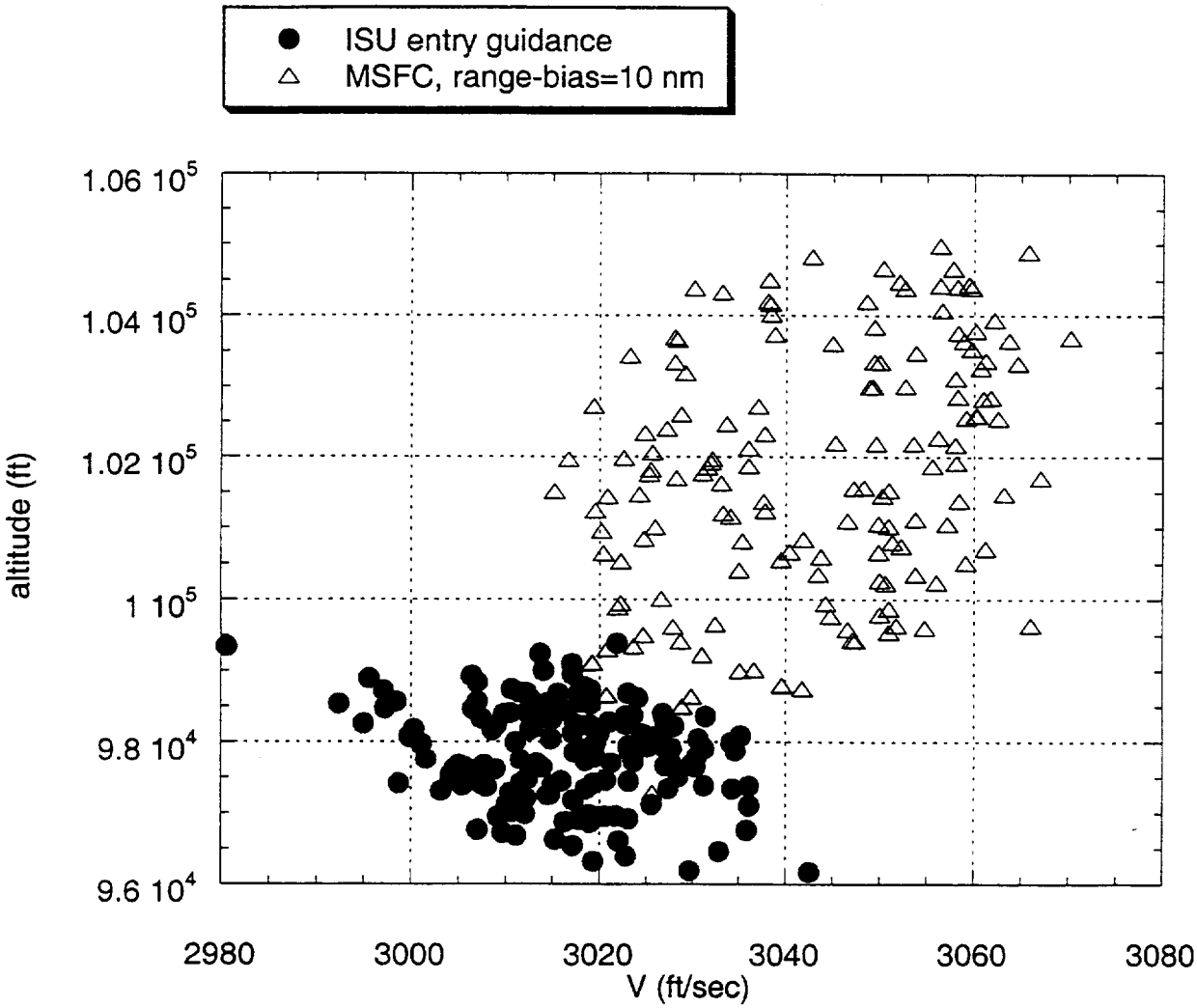

Fig. 22 Velocity and altitude at TAEM for 150 dispersed trajectories

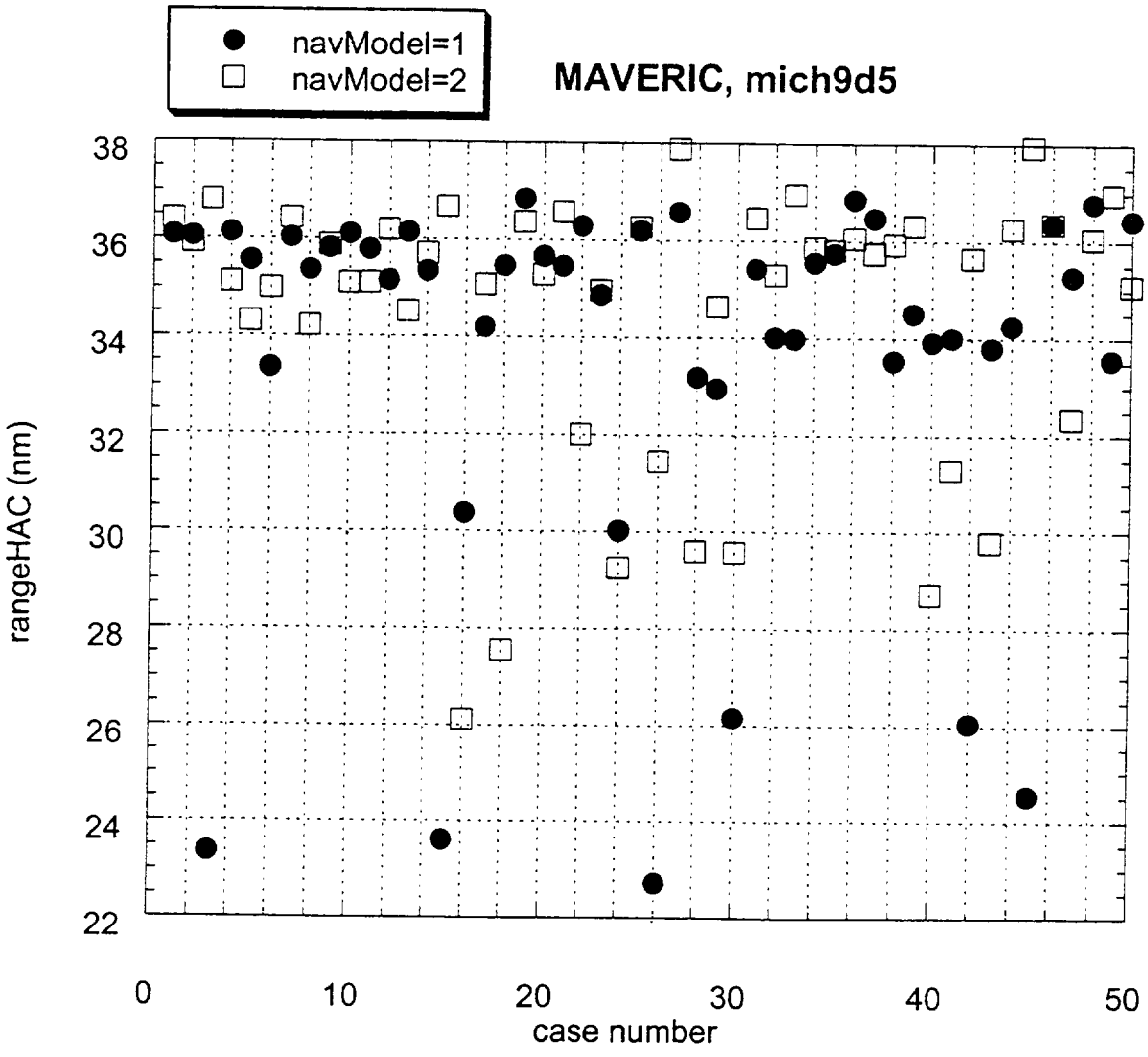

Fig 23 Downrange distance sensitivity (X-33 entry guidance)

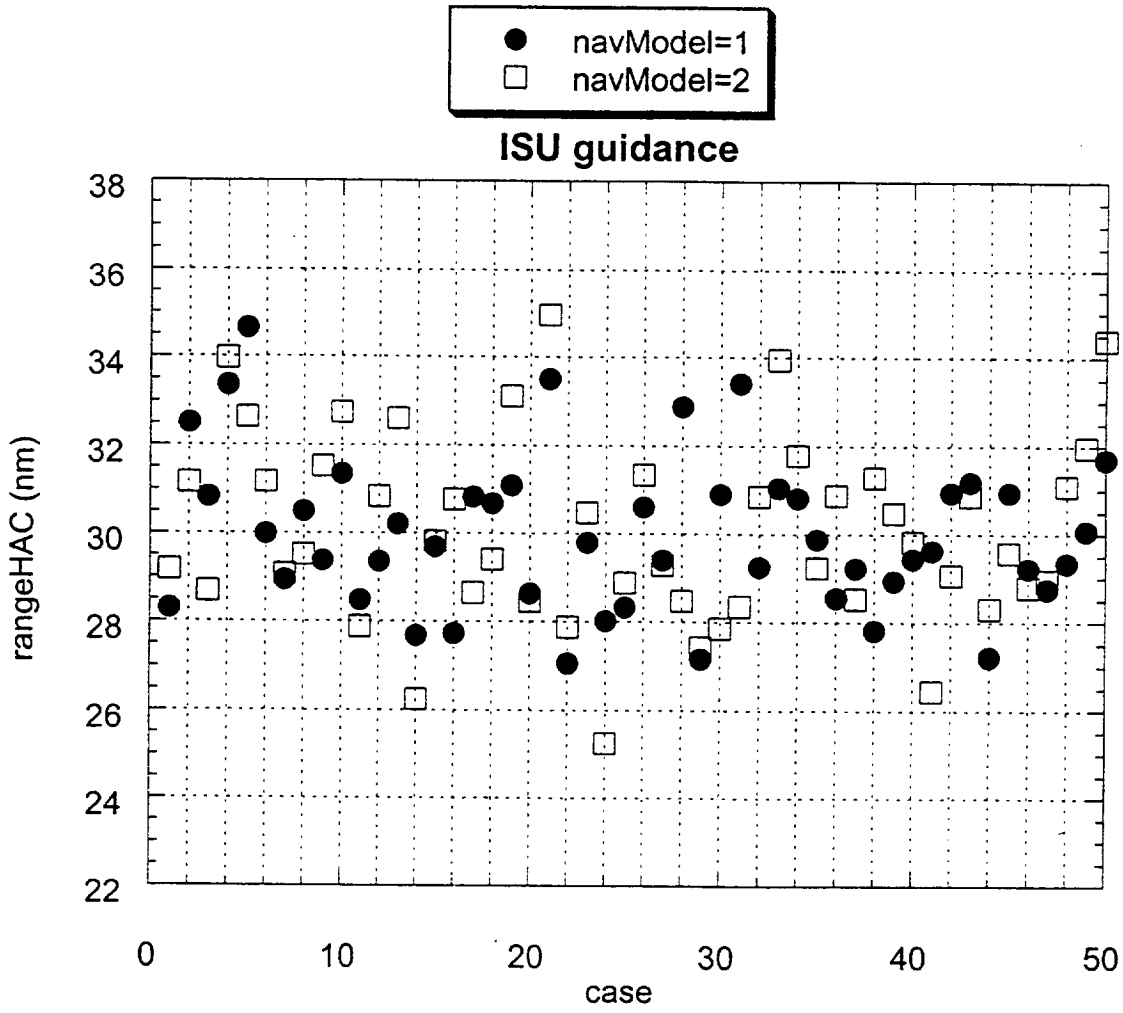

Fig. 24 Downrange distance sensitivity (ISU entry guidance)

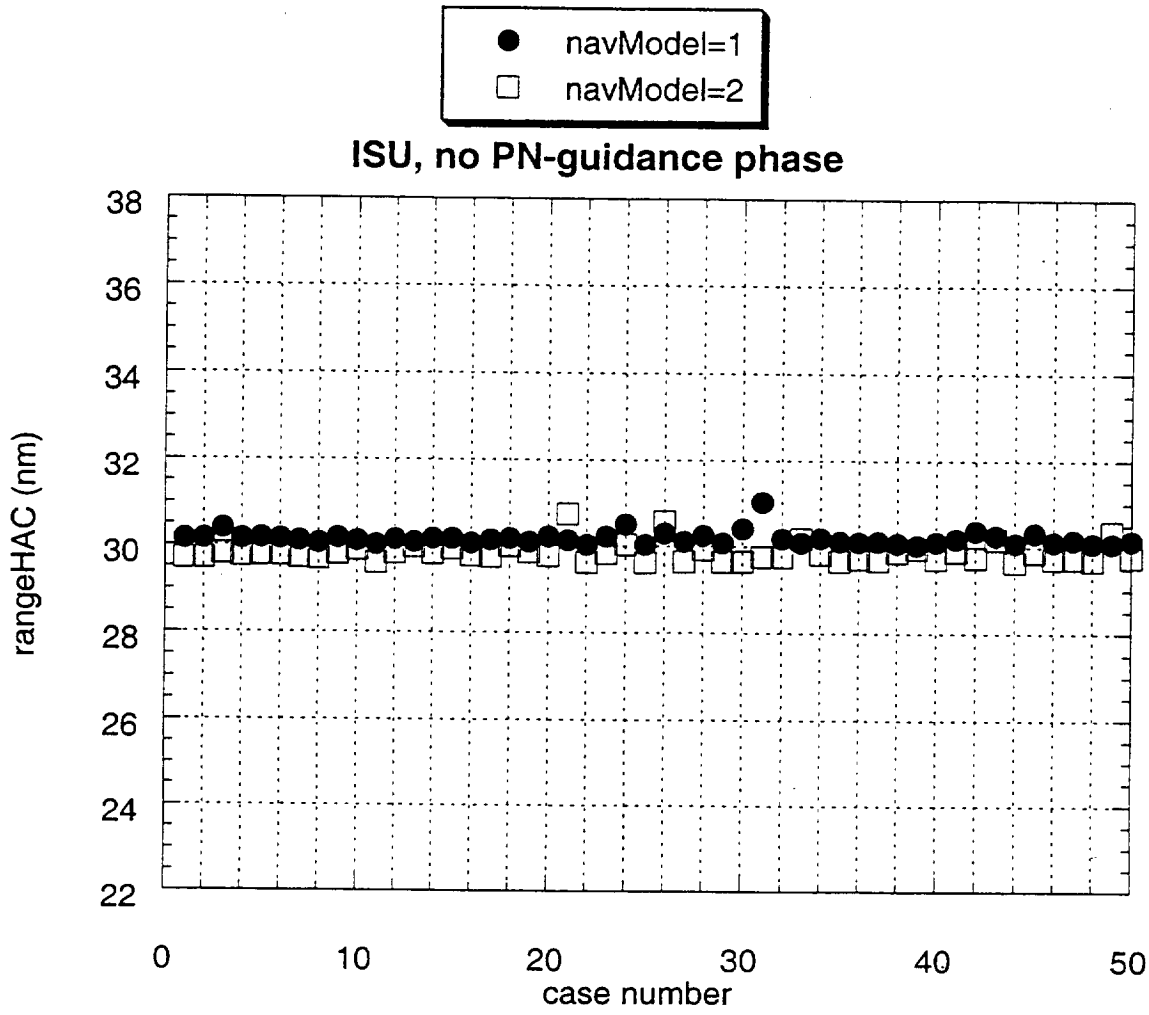

Fig. 25 Downrange distance to HAC at TAEM without pre—TAEM proportional-navigation guidance phase

7. A Candidate for Next-Generation Entry Guidance Method

The entry guidance concept based on drag-profile-tracking has been successful for the Shuttle, and is shown to be effective for the X-33, notwithstanding some additional measures that have to be taken to satisfy the specific entry requirements for the X-33 as described in Section 5. The simulation results in Section 6 are by the most part satisfactory. But if the TAEM condition dispersion specifications are further tighten up, and if more stringent conditions are placed on all trajectory parameters (velocity, altitude, position, and heading), it would be very difficult for the the current entry guidance schemes to achieve all the specifications. The strong trajectory sensitivity observed in Section 6.3 also highlights the fact that much remains to be desired if higher level of precision and tighter trajectory control are required. The next-generation entry guidance method should overcome these shortcomings.

Some preliminary investigation has been conducted in this research effort on this front. The approach taken treats the entry guidance problem as a trajectory-tracking problem in the three-dimensional space. The motivation is simple: since the nominal 3-D entry trajectory has already been carefully designed to satisfy all trajectory constraints and TAEM conditions, and optimize certain performance index in many cases, closely following this trajectory in state-space will automatically ensure a successful mission. The key to the success of this approach is that an effective feedback control law based on the linearized dynamics of the vehicle about the nominal trajectory can be developed to null the deviations from the reference trajectory. One major stumbling block, however, has been the fact that the linearized system is time varying because of the time-varying nature of the reference trajectory. In a sharp contrast to the extensive body of design methods for linear, time-invariant systems, there have been relatively very few available methods for controller design to stabilize a linear, time-varying (LTV) system. A commonly used technique is to design the controller at a number of points along the trajectory, and then interpolate the gains over the flight envelope. Reference [12] presents such an application for entry trajectory control. The practical disadvantages of this technique are that the point designs of the controller and gain scheduling are man-power intensive and highly time consuming, and the entire process has to be repeated for each different reference trajectory for different missions. On an equally (if not more) important note, a fundamental issue is that stability cannot be theoretically guaranteed by such a gain-scheduled controller. Therefore extensive simulations are usually resorted to verify the control law, which further adds to the mission costs.

In a recent work [15], a closed-form stabilizing control law for LTV systems has been developed. The control law is based on an approximation to the solution of a receding-horizon control problem. Once the control law is developed, no on-line integrations or iterations are required. No explicit gain scheduling is used, and the control law has the same form for different reference trajectories. The closed-loop stability of the linearized, time-varying system, hence the stability of the original nonlinear system in a neighborhood of the reference trajectory, is guaranteed for sufficiently small values of a control law parameter. The method is applied to the X-33 entry guidance in simulation. The preliminary results are quite encouraging. In the following this method is briefly described, and some simulation results on the X-33 entry guidance are presented. We refer to Ref. [15] for more detail on the development of the method.

7.1 Approximate Receding-Horizon Control Law

Consider an LTV systems modeled by

$$\dot{x} = A(t)x + B(t)u \tag{67}$$

where $x \in R^n$, $u \in R^m$, and $A(\cdot) : R \to R^{n\times n}$ and $B(\cdot) : R \to R^{n\times m}$ are continuous. A control law $u = K(t)x$ is sought to stabilize the system (67) at the origin for any initial condition $x(t_0)$. The receding-horizon control approach is one of the few existing methods for LTV systems. The receding-horizon control problem at any $t \geq t_0$ is defined to be an optimal control problem in which the performance index

$$J = \int_t^{t+T} [x^T(\tau)Qx(\tau) + u^T(\tau)Ru(\tau)]d\tau \tag{68}$$

is minimized for some $Q \geq 0$ and $R > 0$, subject to system dynamics (67), initial condition $x(t)$, and the terminal constraint

$$x(t+T) = 0 \tag{69}$$

with $0 < T < \infty$. The idea is to solve this optimal control problem in the finite moving horizon $[t, t+T]$ for every $t \geq t_0$. Let $u^*(\cdot)$ be the optimal control obtained in $[t, t+T]$. The applied control at the instant t is set to be $u(t) = u^*(t)$. The process is then repeated for the next t. Note that this receding-horizon control strategy is different from applying $u(\tau) = u^*(\tau)$ for all $\tau \in [t, t+T]$.

Kwon and Pearson[16] show that the solution to this problem for any fixed $T \in [\delta_c, \infty)$ is given by

$$u^*(t) = -R^{-1}B^T(t)P^{-1}(t, t+T)x(t) \triangleq K^*(t)x(t) \tag{70}$$

where $P(t_1, t_2) > 0$ satisfies the matrix Riccati differential equation at any $\tau \in [t, t+T] \triangleq [t, t_T]$

$$-\frac{\partial P(\tau, t_T)}{\partial \tau} = -A(\tau)P(\tau, t_T) - P(\tau, t_T)A^T(\tau) - P(\tau, t_T)QP(\tau, t_T) + B(\tau)R^{-1}B^T(\tau) \tag{71}$$

with the boundary condition

$$P(t_T, t_T) = P(t+T, t+T) = 0 \tag{72}$$

To compute $u^*(t)$ from (70), the Riccati equation (71) needs to be integrated backward from $t+T$ to t with the boundary condition (72). The closed-loop system under control law (70) is uniformly asymptotically stable, provided the system (67) is uniformly controllable.[16]

The need for backward integration of the matrix Riccati differential equation (71) at every instant t poses a serious computational burden for on-line implementation of the control law (70). An analytical approximation to control law (70) may be derived as follows: Consider the above receding-horizon problem in the interval $[t, t+T]$. Divide this interval into N equal subintervals of length $h = T/N$ for some integer $N \geq n/m$. With the current state $x(t)$ known, a first-order prediction of $x(t+h)$ as a function of $u(t)$ is given by a Taylor series expansion at t

$$x(t+h) \approx x(t) + h[A(t)x(t) + B(t)u(t)] = (I + hA)x + hBu \tag{73}$$

Denote $A_k = A(t+kh)$, $B_k = B(t+kh)$, $x_k = x(t+kh)$ and $u_k = u(t+kh)$, $k = 1, ..., N$. Then another first-order Taylor series expansion at $t+h$, together with Eq. (73), gives

$$x(t+2h) \approx x_1 + h[A_1 x_1 + B_1 u_1] \approx (I + hA)(I + hA_1)x + h(I + hA_1)Bu + hB_1 u_1 \quad (74)$$

Continuing this process, we have

$$x_k \approx \Delta_k x + \sum_{i=0}^{k-1} G_{k,i} u_i, \quad k = 1, ...N \quad (75)$$

where

$$\Delta_k = (I + hA_{k-1})\Delta_{k-1}, \quad \text{with } \Delta_0 = I \quad (76)$$

$$G_{k,i} = (I + hA_{k-1})G_{k-1,i}, \; i = 0, 1, ..., k-2, \quad \text{and } G_{k,k-1} = hB_{k-1} \quad (77)$$

The subscript 0 in above expressions denotes the values at t. Let $L_0 = x^T(t)Qx(t) + u^T(t)Ru(t)$ and $L_k = x_k^T Q x_k + u_k^T R u_k$, $k = 1, ..., N$. The integral in Eq. (68) is approximated by the standard trapezoidal formula for integrals:

$$J \approx h(0.5L_0 + L_1 + ... + L_{N-1} + 0.5L_N) \quad (78)$$

Define an (mN)-dimensional vector $v = col\{u(t), u_1, ..., u_{N-1}\}$. If the x_k's in Eq. (78) are replaced by the prediction (75), the performance index is thus approximated by a quadratic function of v:

$$\bar{J} = \frac{1}{2} v^T H(t,h) v + x^T S(t,h) v + q(x,t,h,u_N) \quad (79)$$

where $H \in R^{mN \times mN}$ is positive definite for any t and $h > 0$, $S \in R^{n \times mN}$ and q is quadratic in x and u_N. These terms are obtained directly by rearranging the expression of J in Eq. (78) once x_k's are replaced by Eq. (75). Examples are given in Ref. [15]. The constraint (69) can be approximated by setting $x_N = 0$ from Eq. (75), which can be rewritten in a compact form

$$M^T(t,h) v = -\Delta_N x \quad (80)$$

where

$$M^T = [G_{N,0} \; ... \; G_{N,N-1}] \in R^{n \times mN} \quad (81)$$

The minimization of $\bar{J}$ in Eq. (79) with respect to v subject to constraint (80) constitutes a quadratic programming (QP) problem. For sufficiently small h (equivalently, sufficiently large N for a fixed T), M^T has full rank, given the uniform controllability of the system. Then the above QP problem has a unique solution

$$v = -\left\{ \left[H^{-1} - H^{-1} M \left(M^T H^{-1} M \right)^{-1} M^T H^{-1} \right] S^T + \left[H^{-1} M \left(M^T H^{-1} M \right)^{-1} \right] \Delta_N \right\} x \quad (82)$$

Define an $m \times mN$ matrix

$$I_{mN} = \{ I_{m \times m}, 0, ...0 \} \quad (83)$$

A closed-form, linear, time-varying feedback control law for $u(t)$, denoted by $\bar{u}(t;h)$ hereafter to signify its dependence on time and the value of h, is then obtained from the first m equations in (82)

$$\bar{u}(t;h) = I_{mN} v \triangleq K(t,h) x(t) \quad (84)$$

It can be shown that the difference between control $\bar{u}(t;h)$ and $u^*(t)$ in (70) at the same t is proportional to h. Furthermore, if $A(t)$ and $B(t)$ are bounded with respect to t, for a fixed T, there exists an $h^* > 0$ such that for all $h = T/N \leq h^*$, the closed-loop system under control $\bar{u}(t;h)$ is uniformly asymptotically stable. Or equivalently, for a sufficiently large N, the closed-loop stability is ensured with $h = T/N$. Note that the expression of the control law (84) (the gain $K(t,h)$ in specific) would be different for different values of N. The proof of stability is based on the recognition that the prediction (75) is in fact the Euler integration algorithm applied to system (67) and the trapezoidal formula (19) is a second-order approximation to the integral in (68). The stability conclusion is then obtained from the application of Lyapunov stability theory to the LTV system.

7.2 X-33 Entry Guidance by Trajectory Regulation

Let $x = (r\ \theta\ \phi\ V\ \gamma\ \psi)^T$, and $u = (\sigma\ \alpha)^T$. We will use limited α-modulation as well as for trajectory control. The reference trajectory will be the 3-DOF trajectory found in Section 2. Let $\Delta x(\tau)$ and $\Delta u(\tau)$ denote the differences between the actual and nominal values in x and u. The linearized dynamics of system (1-6) about the reference trajectory are

$$\Delta\dot{x} = A(\tau)\Delta x + B(\tau)\Delta u \tag{85}$$

Both A and B can be obtained analytically. Their elements depend on the state and control histories of the reference trajectory. Applying the control law (84) to the system (85), we have a feedback control law for $\Delta u = K(\tau)\Delta x$, where K is dependent on $A(\tau)$, $B(\tau)$, N and h. The actual trajectory is then controlled by $u(\tau) = u^*(\tau) + \Delta u(\tau)$ with the nonlinear dynamics governed by (1–6), where the asterisk denotes the reference value. The linearized model (85) is only used for control law construction for Δu. Successful trajectory regulation should lead to $\Delta x \to 0$, thus $\Delta u \to 0$, provided the trajectory dispersions are not so large as to invalidate the linearization approximation or cause destabilizing control saturation.

For the system (85), $n = 6$ and $m = 2$. The parameter N in the control law (84) must be at least greater than $n/m = 3$. We have found that any $N \geq 4$ for this application suffices to yield a satisfactory stabilizing control law for Δu. The control law is too lengthy to present here, but otherwise a straightforward matter to obtain by following the systematic formulas given in Section 7.1.

To assess the effectiveness of this guidance method under dispersed conditions, we let the trajectory dispersions at the starting point of the entry flight be randomly distributed in the ranges of

$$\begin{aligned} &|\Delta r(0)| \leq 3 \quad (km), \quad |\Delta\theta(0)| \leq 0.05\ (deg), \ |\Delta\phi(0)| \leq 0.05\ (deg) \\ &|\Delta V(0)| \leq 150 \quad (m/sec), \ |\Delta\gamma(0)| \leq 2\ (deg), \quad |\Delta\psi(0)| \leq 5\ (deg) \end{aligned} \tag{86}$$

These are by no means small dispersions for entry flight. For the trajectory control law employed in the simulations shown in this Report, $N = 8$, $h = 0.02$ (dimensionless, 16 sec in real time), Q =unity matrix, and $R = diag\{5,\ 0.01\}$ (with σ in radian and α in deg) are used. The sizes of $\Delta\sigma$ and $\Delta\alpha$ are bounded by the conditions

$$|\sigma^*(\tau) + \Delta\sigma(\tau)| \leq 90\ (deg) \tag{87}$$

$$|\Delta\alpha(\tau)| \leq \Delta\alpha_{max}(\tau) \tag{88}$$

where $\Delta\alpha_{max}$ is scheduled with respect to Mach number, starting at 5 deg at Mach 10 and linearly increasing to 10 deg at Mach 2.5.

Many trajectories have been simulated, and the results are rather consistent in that all the trajectories have the similar behaviors. Figures 26 and 27 depict the variations of the trajectory dispersions along 10 such trajectories. At the TAEM interface along all the 10 trajectories, the altitude errors are less than 0.2 km, the circular position errors less than 0.7 km, the velocity errors less than 10 m/sec, the flight path angle errors less than 1 deg, and the heading angle errors less than 1 deg. This level of accuracy represents a major improvement in the precision that trajectory control can achieve in the context of entry guidance. It would be possible for the the drag-tracking guidance approach to attain similar accuracy in some (no more than half) of the state variables, but certainly not the level of overall precision demonstrated here. This conclusion is evident when one compares Figs. 16–19 with Figs. 26–27. It should be noted that no navigation uncertainty is considered in above assessment.

The variations of complete σ and α (not just dispersions) along those 10 trajectories are shown in Fig. 28. It can be seen that as the trajectory dispersions are reduced by the feedback control law, the bank angle and angle of attack return to their nominal values.

Remarks

1. Although the independent variable used in above discussion is the time, it is not a necessity. In fact, if the use of some other monotonic variables (e.g., energy) as the independent variable in defining the reference trajectory is deemed to be more advantageous, the methodology has no difficulty to apply to such a case. Note that the linearized system equation (85) (A and B matrices in particular) will be different if a different independent variable is used, therefore the control law must be reformulated accordingly.

2. Both the Shuttle and X-33 entry guidance also use α-modulation for better tracking performance, particularly during bank reversals. Without α compensation, bank reversals tend to degrade significantly the trajectory control accuracy. The current approach provides coordinated and continuous σ and α modulation commands that do not call for sudden changes (reversals). Furthermore, the approach is uniform in that no separate considerations are needed for longitudinal and lateral trajectory control.

3. The tightness of the trajectory control depends directly on the control margins available, i.e., the allowable sizes of $\Delta\sigma$ and $\Delta\alpha$. The larger the margins are, the higher controller gain (smaller h parameter) may be used for tighter trajectory control, or the larger trajectory dispersions can be accommodated for the same controller gain. When we keep increasing the magnitudes of trajectory dispersions to the point when divergence occurs, it is always inevitably due to control saturations.

4. Some simple tests have also been done on the robustness of the trajectory control law with respect to aerodynamic uncertainties. One of the noted advantages of the receding-horizon control is its robustness. In this entry guidance application, the preliminary finding suggests again that robustness is strongly dependent on the available

control margins. With larger margins, more substantial uncertainties can be compensated by the feedback control law. No effort has been made yet on comparing the robustness of the drag-tracking guidance strategy of the Shuttle/X-33 and the current method. But our conjecture is that when the control margins are severely limited, the drag-tracking approach will probably be more robust, because the current approach attempts to regulate all the state variables rather than track just one function of the state.

5. The performance of the control law is very insensitive to the choice of the Q matrix. The choice of the R matrix has more noticeable effect in balancing the relative magnitudes of $\Delta\sigma$ and $\Delta\alpha$, but far from being highly critical.

This trajectory-regulation method obviously requires a larger software for the trajectory control law compared to the drag-tracking approach, though it may not be an issue with the capability of the current generation of flight computers. More extensive evaluations, preferably with high-fidelity vehicle simulation programs such as MAVERIC, remain to be done to further determine feasibility, robustness, and versatility of this approach. But if the above preliminary results are any indication, this method should be a very promising candidate of entry guidance scheme in missions where high precision is critical.

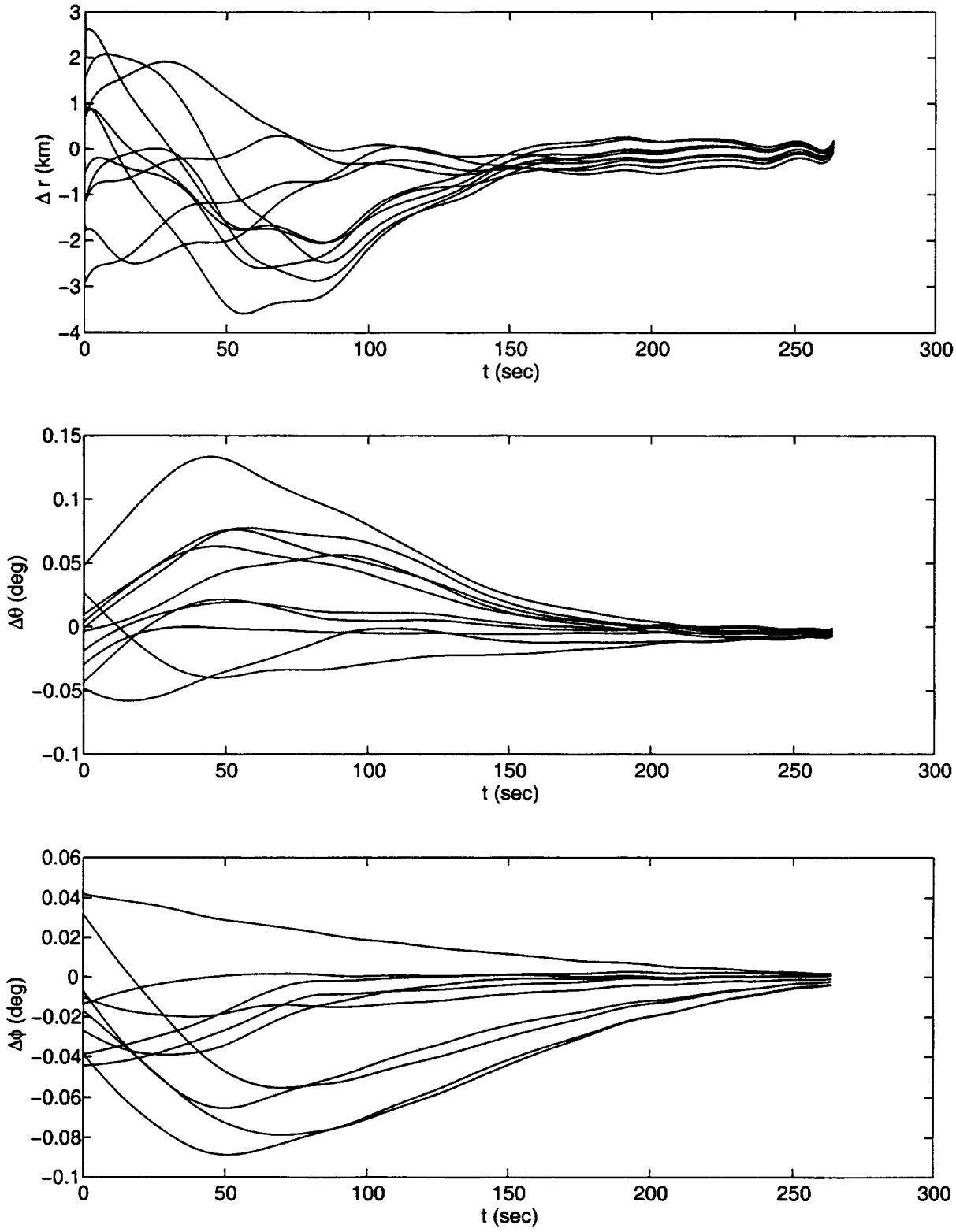

Fig. 26: Dispersions in altitude, θ and ϕ

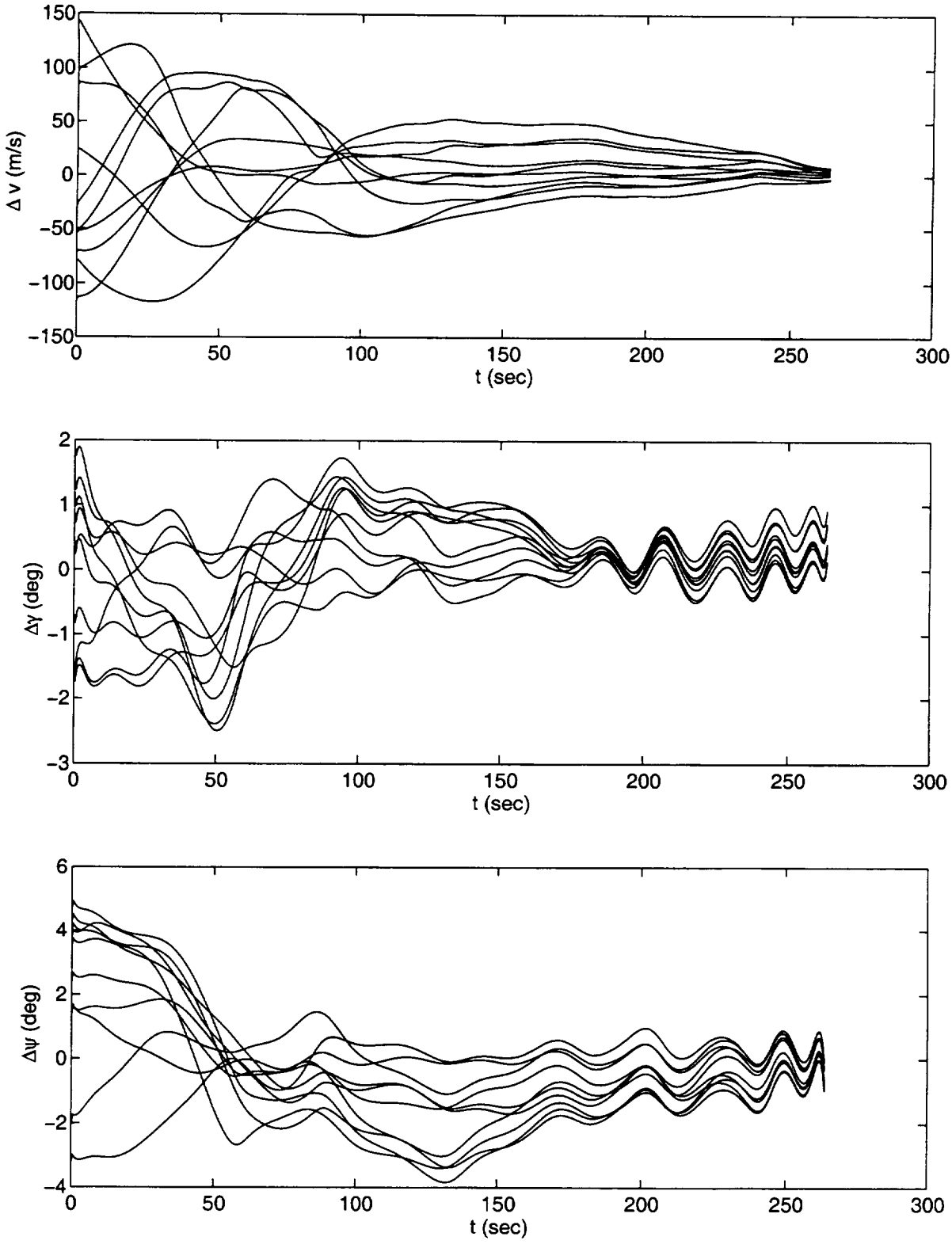

Fig. 27: Dispersions in v, γ and ψ

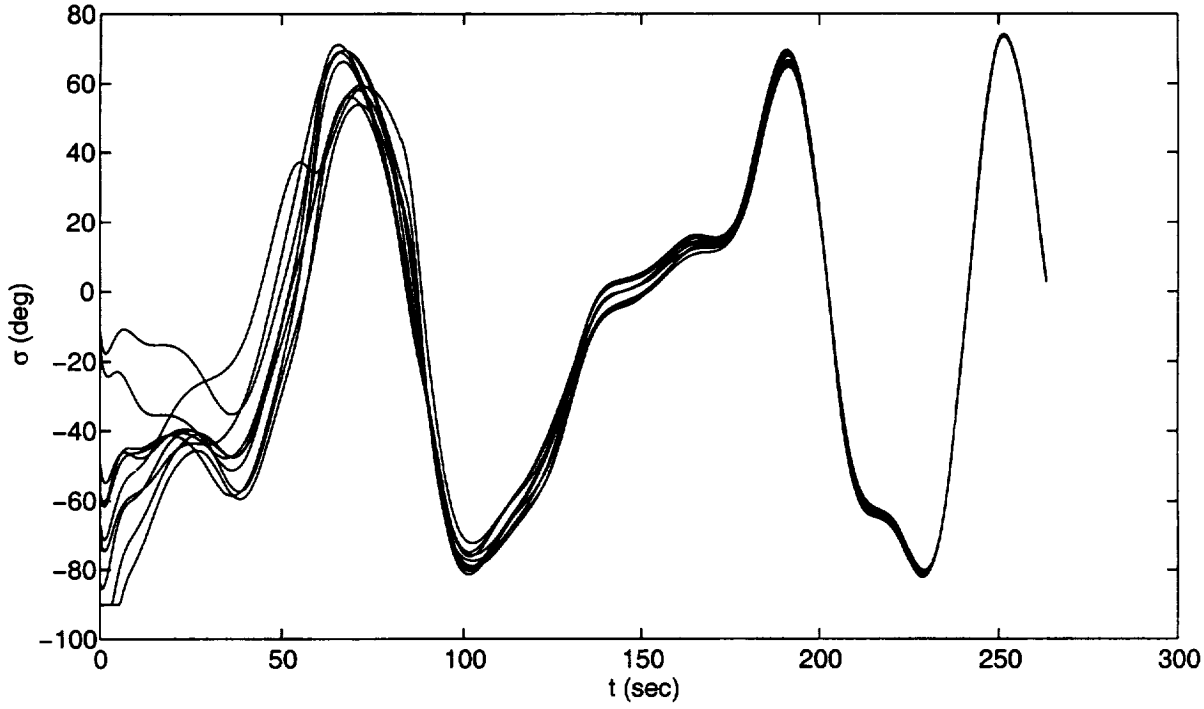

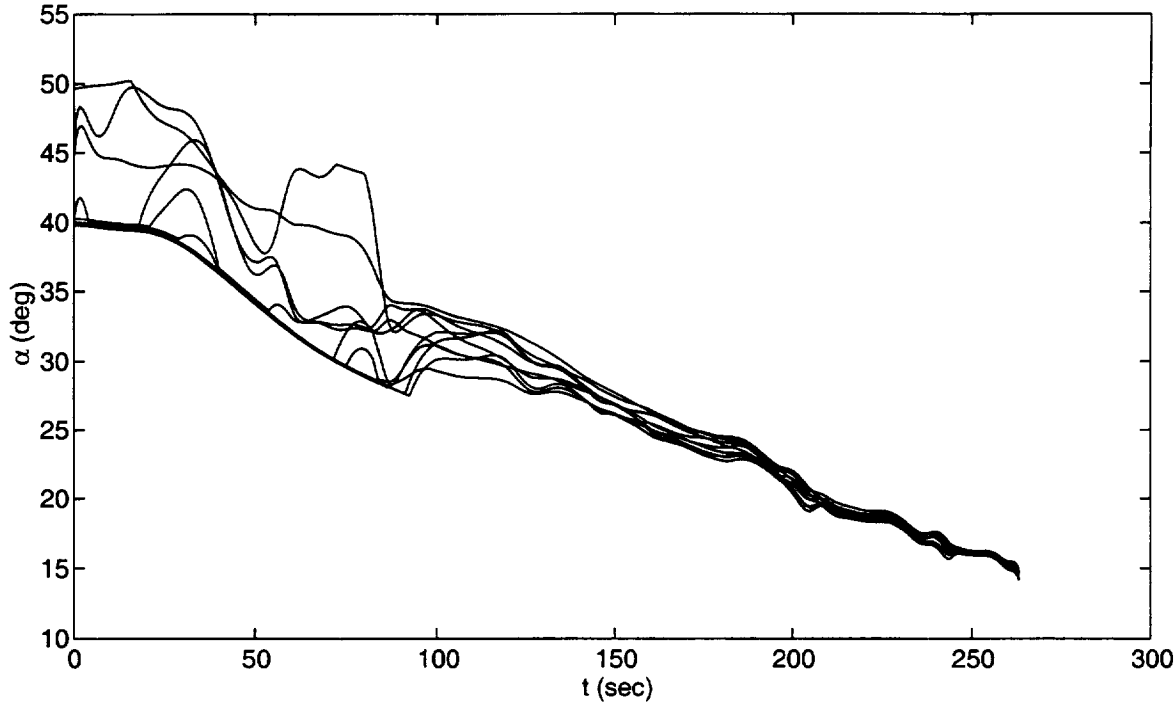

Fig. 28: Variations of dispersed σ and α

8. Summary and Conclusions

This research was conceived to develop an alternate entry guidance scheme for the X-33 vehicle in parallel to the on-going development of the actual X-33 entry guidance algorithms, provide comparative evaluation of the two methods, and complement the actual X-33 entry guidance design whenever appropriate. Other goal of this research were to identify new ways that can potentially improve entry guidance system performance, reduce the cost/labor associated with entry guidance development, and enhance the capability of entry guidance system. This research has resulted in 5 publications in scholarly journals and proceedings of professional conferences[7, 9, 10, 13, 15] which document much of the progress and results of this research. These contributions to literature can be divided into two categories: those that are directly focused on entry guidance for the X-33 [7, 9, 10], and those that develop general approaches and impact on entry guidance methodology.[13, 15] This report summarizes the new developments in entry guidance design stemming from the X-33 application. These new techniques combined with the Space Shuttle entry guidance principle have contributed to an improved and effective entry guidance scheme for the X-33. In the same time, the limitations of Shuttle-based entry guidance methods are identified. The lessons learned and experience gathered in the X-33 entry guidance design have motivated research on next-generation of entry guidance methods that will be more capable and adaptive.

References

[1] Harpold, J. C., and Graves, C. A., "Shuttle Entry Guidance," *The Journal of the Astronautical Sciences*, Vol. XXXVII, No. 3, 1979, pp. 239–268.

[2] Dukeman, G. A., and Gallaher, M. W., "Guidance and Control Concepts for the X-33 Technology Demonstrator", paper AAS-98-026, 21st Annual AAS Guidance and Control Conference, Feb. 4-8, 1998, Breckenridge, CO.

[3] Coughlin, D., Dukeman, G., Hanson, J., Mulqueen, J., and McCarter, J., "Ascent, Transition, Entry, and Abort Guidance Design for the X-33 Vehicle", AIAA paper-98-4409, *Proceedings of Guidance, Navigation, and Control Conference*, August 10–12, 1998, Boston, MA.

[4] Vinh, N. X., Busemann, A., and Culp, R. D., *Hypersonic and Planetary Entry Flight Mechanics*, The University of Michigan Press, Ann Arbor, MI, 1980.

[5] Regan, F. J., and Anandakrishnan, S. M., *Dynamics of Atmospheric Re-Entry*, AIAA Education Series, 1993.

[6] Zhou, J. L., Tits, A. L., and Lawrence, C. T., "User's Guide for FFSQP Version 3.7: A FORTRAN Code for Solving Constrained Nonlinear (Minimax) Optimization Problems, Generating Iterates Satisfying all Inequality and Linear Constraints", Systems Research Center TR-92-107r2, the University of Maryland, April, 1997.

[7] Lu., P., and Hanson, J., "Entry Guidance for the X-33 Vehicle", *Journal of Spacecraft and Rockets*, Vol. 35, No. 3, 1998, pp. 342–349.

[8] Lu, P., "Entry Guidance and Trajectory Control for Reusable Launch Vehicle", *Journal of Guidance, Control, and Dynamics*, Vol. 20, No. 1, 1997, pp. 143–149.

[9] Lu, P., and Hanson, J., "Entry Trajectory Design for the X-33", *Proceedings of the AIAA Atmospheric Mechanics Conference*, August 11–13, 1997, New Orleans, LA.

[10] Lu, P., Hanson, J., Dukeman, G., and Bhargava, S., "An Alternative Entry Guidance Scheme for the X-33", *Proceedings of the AIAA Atmospheric Mechanics Conference*, August 10–12, 1998, Boston, MA.

[11] Hill, A., Anderson, D., Coughlin, D., and Chowdhry, R., "X-33 Trajectory Optimization and Design" AIAA paper-98-4408, *Proceedings of Guidance, Navigation, and Control Conference*, August 10–12, 1998, Boston, MA.

[12] Roenneke, A. J., and Markl, A., "Reentry Control of a Drag versus Energy Profile", *Journal of Guidance, Control, and Dynamics* , Vol. 17, No. 5, 1994, pp. 916–920.

[13] Lu, P., "Intercept of Nonmoving Targets at Arbitrary Time-Varying Velocity", *Journal of Guidance, Control, and Dynamics*, Vol. 21, No. 1, 1998, pp. 176–178.

[14] Lu, P., "A Further Look at X-33 Entry Guidance and Beyond", Final Report, NASA/ASEE Summer Faculty Fellowship Program, NASA Marshal Space Flight Center, August 1999.

[15] Lu, P., "Regulation about Time-Varying Trajectories: Precision Entry Guidance Illustrated", to appear in *Journal of Guidance, Control, and Dynamics*, 1999

[16] Kwon, W. H., and Pearson, A. E., "A Modified Quadratic Cost Problem and Feedback Stabilization of a Linear System." *IEEE Trans. on Automatic Control*, Vol. 22, 1977, pp. 838–842.